

Photoinduced Charge Dynamics in Indoline-Dye Sensitised Solar Cells

by

Iulia Minda

*Thesis presented in partial fulfilment of the requirements for the degree
of Master of Science in Laser Physics in the Department of Physics at
Stellenbosch University*



Department of Physics,
University of Stellenbosch,
Private Bag X1, Matieland 7602, South Africa.

Supervisors:

Prof Heinrich Schwoerer	Prof Derck Schlettwein
Laser Research Institute Stellenbosch University	Institut für Angewandte Physik Justus-Liebig-Universität Gießen

December 2014

Declaration

By submitting this thesis electronically, I declare that the entirety of the work contained therein is my own, original work, that I am the sole author thereof (save to the extent explicitly otherwise stated), that reproduction and publication thereof by Stellenbosch University will not infringe any third party rights and that I have not previously in its entirety or in part submitted it for obtaining any qualification.

Date:

Copyright © 2014 Stellenbosch University
All rights reserved.

Abstract

Photoinduced Charge Dynamics in Indoline-Dye Sensitised Solar Cells

I. Minda

*Department of Physics,
University of Stellenbosch,
Private Bag X1, Matieland 7602, South Africa.*

Thesis: MSc

December 2014

The demand for renewable energy sources has grown out of the humanity's increasing need for electricity as well as depleting fossil fuel reserves. Organic-dye sensitised solar cells were developed as a green, cost-effective alternative to the market-dominating silicon solar cell technology. The field of photovoltaic devices and organic-DSSCs is interesting because we want to develop better, more efficient cells at lower costs using environmentally friendly materials. By studying the fundamental physics and chemistry processes occurring during and after the interaction of light with these devices, we create a window into the mechanism of photosynthesis. Our DSSCs were prepared by sensitisation of highly porous ZnO with different indoline dyes containing the same chromophore, but different alkyl chain lengths bonded to one of two carboxyl anchors as: DN91 (1 C) < DN216 (5 C) < DN285 (10 C). The role of the dye molecules is to absorb photons and donate electrons to the ZnO which acts as the charge acceptor, at the dye|ZnO interface. Through photoelectrochemical characterisation it was found that the structure of the dyes has an effect on the maximum current (J_{SC}) produced by the cells: the shorter the alkyl chain, the higher the J_{SC} . This macroscopic investigation was complimented by microscopic measurements in the form of transient absorption spectroscopy. This allows us to follow, in real time, the photoinduced oxidation of the dye and its regeneration occurring through desired and undesired pathways. It was found that the injection efficiencies of the dye molecules were directly responsible for the trend in the short circuit currents.

Uittreksel

Liggeïnduseerde Ladingdinamika in Indolien-Kleurstof Gesensitiseerde Sonselle

(“Photoinduced Charge Dynamics in Indoline-Dye Sensitised Solar Cells”)

I. Minda

*Departement Fisika,
Universiteit van Stellenbosch,
Privaatsak X1, Matieland 7602, Suid Afrika.*

Tesis: MSc

Desember 2014

Die aanvraag na die ontwikkeling van herwinbare energie bronne spruit voort uit die voor-sienbare uitputting van fossiel brandstof bronne sowel as die groeiende behoefte om aan die mensdom se elektrisiteit behoeftes te voldoen. Kleurstof gesensitiseerde sonselle is ontwikkel as 'n groen, koste-effektiewe alternatief tot die silikon sonsel tegnologie wat die mark domineer. Die fotovoltaise toestel veld, spesifiek organiese kleurstof gesensitiseerde sonselle is interessant omdat daar ruimte bestaan vir die ontwikkeling van beter meer effektiewe selle in terme van vervaardigings koste en prosesse wat omgewingsvriendelik is. Deur die fundamentele fisika en chemiese prosesse wat plaas vind tydens en na lig interaksie met hierdie selle te bestudeer gee dit insig oor die werkingsmeganisme van fotosintese. Ons kleurstof gesensitiseerde sonselle is voorberei deur sensitisasie van hoogs poreuse ZnO met verskillende indolien kleurstowwe wat dieselfde kromofoor bevat wat met verskillende alkiel ketting lengtes verbind is aan een van twee karboksiel ankers as: DN91 (1 C) < DN216 (5 C) < DN285 (10 C). Die rol van die kleurstof molekules is om fotone te absorbeer en elektrone te doneer aan die ZnO wat as die lading akseptor dien by die kleurstof/ZnO intervlak. Deur fotoelektrochemiese karakterisasie is bevind dat die struktuur van die kleurstof 'n effek het op die maksimum stroom (J_{SC}) wat die selle produseer: hoe korter die die alkiel ketting, hoe hoër die J_{SC} . Hierdie makroskopiese ondersoek is voltooi deur mikroskopiese metings in die vorm van tydopgelosde absorpsiespektroskopie. Dit laat ons toe om die fotogeïnduseerde oksidasie asook regenerasie van die kleurstof te volg soos wat dit plaas vind deur gewenste sowel as ongewenste roetes. Dit is bevind dat die inspui-tings effektiwiteit van die kleurstof molekules direk verantwoordelik is vir die waarneembare trajek in die kortsluitings stroom.

Acknowledgements

I would like to first thank my supervisor, Prof. Heinrich Schwoerer, for not only teaching me all I know about transient absorption spectroscopy, but also for the guidance and patience over the last two years. Your passion for experimental physics rubs off on all of us around you. Thank you for being so approachable and for creating a wonderful research environment for us to learn in.

Thank you also to my co-supervisor, Prof. Derck Schlettwein, as well as the rest of the group in Gießen, Germany. Firstly for providing us with samples, but also for welcoming me as a part of your group for 5 months. Especially Christoph Richter, thank you for teaching me how to make my own solar cells and helping me in the lab. My time spent in Gießen was an excellent learning experience as well as a unforgettable life experience.

Dr. Egmont Rohwer, thank you for sharing your knowledge of transient absorption spectroscopy with me. Not only in the lab, but also interpreting of results as well as answering my many questions. Gabriele Tauscher, thank you for all the help in the lab and struggling alongside me while we learnt to take transient measurements. Thank you to my entire research group. I am so glad to be part of such a great team and so grateful that I can share this journey with you.

I'd like to thank my family and friends for all the support and prayers over the years. Thank you to my parents and sister for creating a curious spirit within me and teaching me to see life as a series of adventures. Charles Abernethy, I hope that through this thesis you see that physicists don't just solve equations of motion all day. I thank you for all your love and support. Thank you God for yet another great adventure.

Finally, I'd like to thank the National Research Foundation (NRF) and the South African Research Chair initiative for the generous financial assistance over the last two years.

Contents

Declaration	i
Abstract	ii
Uittreksel	iii
Contents	v
1 Motivation	1
2 Introduction to DSSCs	2
2.1 Different Types of Solar Cells	2
2.2 Dye Sensitised Solar Cells	2
3 Preparation of DSSCs	8
3.1 Electrodeposition of ZnO	8
3.2 Adsorption of Organic Dye	9
3.3 Building the Solar Cell	10
3.4 Photoelectrochemical Characterisation	12
4 Femtosecond Transient Absorption Spectroscopy	16
4.1 A Typical Spectrum	16
4.2 Pump-Probe Spectroscopy	19
5 Transient Absorption Measurements	30
5.1 Transient Absorption Spectra	30
5.2 Horizontal Lineouts	33
5.3 UTA Measurements on D149 Sensitised Solar Cells	39
5.4 Spectral Shift	40
5.5 Applied Voltage Measurements	40
6 Conclusion	42
Appendices	44
A Experimental Details of Fabrication of DSSCs	45
B Self Phase Modulation	46
Bibliography	48

1. Motivation

As the Earth's population grows and our lives become more technology dependent, electricity generated through non-renewable paths is no longer keeping up with the ever-increasing energy demand. The projected power usage is 28 TW for 2050, compared to 13 TW in 2000 [1]. Fossil fuels are a limited resource, therefore we need to focus our attention on renewable energy sources. In this way we can plan how to satisfy the Earth's energy needs, but not at its own expense. The Sun provides us with a constant supply of energy. Which, if harnessed in a safe, cost-effective, green and commercially viable way, could have great potential to fill the energy gap. It is measured that approximately 1.7×10^5 TW of solar power reaches the Earth, of which it is estimated that 60 TW of power could be generated from solar farms, assuming 10% efficiency [1]. As there is a supply of energy, the search for efficient, green, cheap and long-lasting photovoltaic devices which can convert solar energy to electrical energy is ongoing. So far, most of the weight is being carried by silicon solar cells as they are efficient and durable. Various solar cells using organic materials, amongst them dye sensitised solar cells (DSSCs) were developed and improved over the last 25 years as alternatives to silicon solar cells – not to replace them, but to respond to the growing need for photovoltaic devices which can easily be implemented into industries as well as daily life as a substitute to fossil fuels [2].

As scientists, the field of photovoltaic devices and organic-DSSCs is interesting. Firstly, because we want to be able to develop better, more efficient cells at lower costs using environmentally friendly materials. Additionally, because we want to understand the fundamental physics and chemistry processes occurring during and after the interaction of light with these devices, which are similar to what happens in one of nature's most amazing elementary processes, photosynthesis. In a similar way to a green leaf, the colourful dye molecules used in a DSSC, absorb light, transfer charges and energy and generate a dipole moment.

To achieve this, we learn from the DSSCs already developed, as well as the various types of spectroscopic and photoelectrochemical measurements which others have taken before us, and build on the knowledge they have acquired. To explore the electrochemical properties of the cells, we make dye sensitised cell samples using different methods as well as various organic dyes and electrolyte solutions and measure how they behave macroscopically based on these controlled changes. In addition, we use experimental methods available to us such as transient absorption spectroscopy (TAS) to learn more about the microscopic properties of the cells. From the TAS measurements, we are able to monitor the change in the cells', and more specifically the dye molecules', absorption over time as transient signals and apply this information to learn about the evolution of excited molecules and semiconductors, and photoinduced charge dynamics present in the charge transfer processes. By describing the changes in absorption over time with analytical decay functions, we extract decay time constants and relative amplitudes and determine electron paths within the cells. So, together with literature studies we build models, based on our results as well as others' results and models, about the paths that electrons follow, with which time constants these processes occur and the relative amount of electrons following a certain path. Specifically in the context of solar cells made with various indoline-dye sensitised ZnO thin films. As part of the study I carried out the photoelectrochemical measurements and sample preparation in Gießen, Germany, and the spectroscopy in Stellenbosch, South Africa. Our measurements then bring us a step closer to understanding the details behind the way in which these specific DSSCs function as well as what can be done to better them for future applications and broaden our understanding of light harvesting processes which occur in nature.

2. Introduction to DSSCs

As the Earth's focus shifts towards renewable resources for a supply of energy, research in the field of solar power is valuable and has attracted much attention. The currently developed photovoltaic cells can be separated into many categories, of which silicon based solar cells, dye sensitised solar cells and organic solar cells are just three [3]. In addition, organic-inorganic hybrid cells which contain a perovskite compound have sparked an interest in the photovoltaic research community most recently. Some of these cells will be introduced briefly in this work, but the focus will be placed on dye sensitised solar cells, their production and electrochemical characterisation, as well as the measurement of photoinduced electron dynamics which take place within the cells, under various conditions.

2.1 Different Types of Solar Cells

Currently, silicon solar cells are the leading type of photovoltaic devices. This is due to their high efficiencies of 25% [4] and long term stability as well as the ease of commercial production. The working principle of crystalline silicon solar cells is based on a highly pure silicon wafer. Upon recrystallisation, a junction forms between the p-type-Si and the n-type-Si due to impurity segregation. In this way the p-type-Si becomes positively charged due to excess holes and the n-type-Si negatively charged due to the excess electrons. Upon illumination, the creation of another electron-hole pair creates an electric field at the junction and charge separation occurs as a result causing the electrons and holes to migrate towards the contacts to the external circuit [5]. The photoexcitation and charge separation processes both occur within the same bulk material in the case of silicon solar cells.

As alternatives to silicon based photovoltaic devices, a number of different solar cells have been developed for research purposes with a commercial interest. So far, one of the photochemical cells that have come close to reaching the commercial feasibility of Si based solar cells, have been organic-inorganic hybrid solar cells containing a perovskite compound introduced by Kojima, *et al.* in 2009 [6]. These cells are highly reproducible and the record efficiency achieved to-date is 17.9% [4]. Their working principle was based on the one of dye sensitised solar cells, which will be explained in detail below, and uses the perovskite compound ($\text{CH}_3\text{NH}_3\text{PbI}_3$) as the light absorber, a semiconductor (TiO_2 or ZnO) as the electron acceptor and a hole conducting material, such as *spiro*-OMeTAD, as the hole acceptor for the charge separation process. Therefore, in this case the photoexcitation and charge separation occur in different materials [7; 8].

2.2 Dye Sensitised Solar Cells

Function

The dye sensitised solar cell has the same function as the above-mentioned photovoltaics – that of conversion of energy from light into electricity. It can be produced simply and cheaply as well as with the use of abundant materials. The maximum efficiency achieved to-date is 13% although in an eight-parallel-cell mini module, efficiencies close to 30% have been reached [4; 9].

Dye sensitised solar cells convert solar energy to electricity through the use of a dye, in a process similar to photosynthesis. The working electrode of a DSSC is made up of a light harvesting material, a dye, which is adsorbed onto a semiconductor surface. The dye is

photoexcited and electrons are injected into the semiconductor whereby they can be harvested into the outside circuit to the counter electrode. The circuit of the cell is usually closed with the use of a liquid electrolyte consisting of a redox couple. A redox couple refers to two ions that work together in a solution to keep their environment neutral, one with a higher negative charge than the other, in this instance I^- and I_3^- . The more negative ion will donate an electron to reduce an oxidised species and in turn be oxidised. The iodide/triiodide system is the most commonly employed redox couple in DSSCs as both the reduction of the dye by I^- is fast enough and the subsequent reduction of I_3^- at the cathode is slow enough to ensure efficient dye regeneration as well as high charge collection [10]. As alternatives, organic redox couples, transition metal complexes and solid hole conductors have been used as replacement for the iodide/triiodide system [11; 12].

To ensure that a maximum number of electrons are injected into the semiconductor, the dye is adsorbed as a monolayer. Aggregates increase the path length from the photoexcited molecule to the semiconductor surface thereby impairing the injection of electrons, see figure 2.1 [13]. With that said, if the semiconductor was a tightly packed layer, a very small surface could be sensitised and the absorption cross section would be very low. Therefore to ensure that there is a largest possible surface area available for the dye monolayer to adsorb to, the semiconductor is built up as a highly porous nano-particle structure. The implementation of using a highly porous semiconductor by O'Regan and Grätzel revolutionised DSSCs in 1991, by increasing their efficiency from 1% to above 7% [14].

Although similar to other photovoltaics, DSSCs have a different working principle. In other words, the charge separation within the cell occurs through different processes [15].

Figure 2.2 shows the electron kinetics within a dye sensitised solar cell. In the dye, the electrons absorb light of a fixed energy and are photoexcited from the highest occupied molecular orbital (HOMO) to the lowest unoccupied molecular orbital (LUMO) following the process marked 1. From this singlet excited state, S^* , the electrons have two possible paths. Either they are injected into the conduction band (CB) of the semiconductor or into an intermediate surface trap state, in the case that the semiconductor is ZnO, as indicated by process 2. The injected electrons then diffuse to the anode before being harvested to the external circuit. The injection process causes the generation of oxidised dye molecules which are in turn reduced by the redox couple (process 3). The redox couple itself is regenerated at the cathode (process 4). These processes are marked in green in figure 2.2 and they are favourable in terms of cell optimisation. The counter processes are marked in blue, and they are as follows: arrow 5 indicates a relaxation of the photoexcited electrons back to the ground state of the neutral dye and arrows 6 and 7 represent the recombination processes which can take place after injection has already taken place, with the oxidised dye and with the redox couple, respectively. Each of the paths depicted in figure 2.2 has a characteristic lifetime associated with it – some processes occur on the femtosecond time scale while others on the nanosecond time scale. Therefore different methods of measuring these lifetimes must be used.

The potential difference between the quasi-Fermi level of the semiconductor under illumination and the redox couple Nernst potential determines the maximum voltage producible with the dye sensitised solar cell. This value is also commonly known as the open circuit voltage of the DSSC, V_{OC} , and although it seems to be independent of the dye used as a

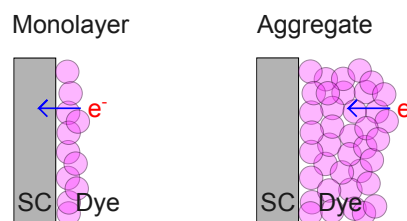


Figure 2.1: Photoexcited electron injection from dye monolayer to semiconductor and retardation of injection of photoexcited electron due to dye aggregate.

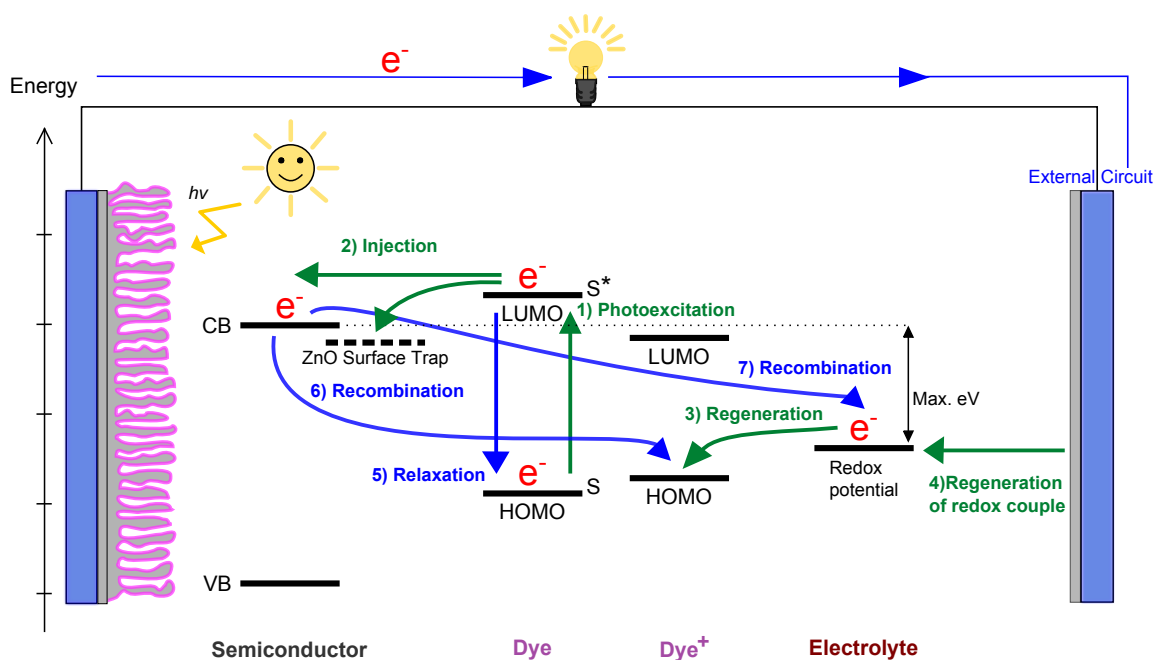


Figure 2.2: Schematic of electron paths within a DSSC. The green arrows show paths favourable to cell optimisation, and the blue arrows show processes unfavourable to cell optimisation.

sensitiser, studies have been carried out where the acidity of the dye affects the V_{OC} [16; 17].

ZnO as an Alternative to TiO₂

As already mentioned, the pioneering dye sensitised solar cells were developed by Michael Grätzel and his team and for this reason they are often referred to as Grätzel cells. The initial design uses TiO₂ as the semiconductor and a trimeric ruthenium complex as the sensitiser. The DSSCs were made as sandwich cells between two fluorine doped tin oxide (FTO) coated glass slides. For the nano-porous semiconductor structure, a TiO₂ nano-particle paste was spread onto the conductive side of the glass slide. In order for the paste to dry and set, the thin film was sintered at a temperature of 450°C [14]. This high temperature baking unfortunately limits the substrates onto which TiO₂ DSSCs can be built to strong, mechanically rigid and high temperature resistant.

The dye sensitised solar cells used in this work are different to the original Grätzel cells as the semiconductor used for the highly porous thin film is ZnO. ZnO is a good alternative to TiO₂ as it has a similar band gap of 3.2-3.4 eV, higher charge carrier mobility and many nanostructure possibilities [18]. Also, it can be electrodeposited as a highly porous nano-particle thin film at a low temperature of 70°C. The fact that no high temperature sintering is necessary means that ZnO thin films can be deposited on mechanically flexible substrates such as plastics therefore reducing the price and increasing the versatility of the DSSCs. Similarly to TiO₂, ZnO thin films can also be made with the use of the Sol-gel method and high temperature sintering although the ZnO thin films are not very reproducible and it eliminates the main benefit of ZnO over TiO₂ as a semiconductor in DSSCs. Due to the chemical properties of ZnO it cannot be sensitised with such an acidic dye such as the initially used ruthenium complex. Additionally, Ru is expensive and rare, therefore ruthenium complex dyes must be replaced if we are to make cost efficient and environmentally friendly solar cells. Indoline dyes, in addition to being fully organic and having high molecular extinction coefficients, are fairly inexpensive due to their simple synthesis procedure and lack of metal

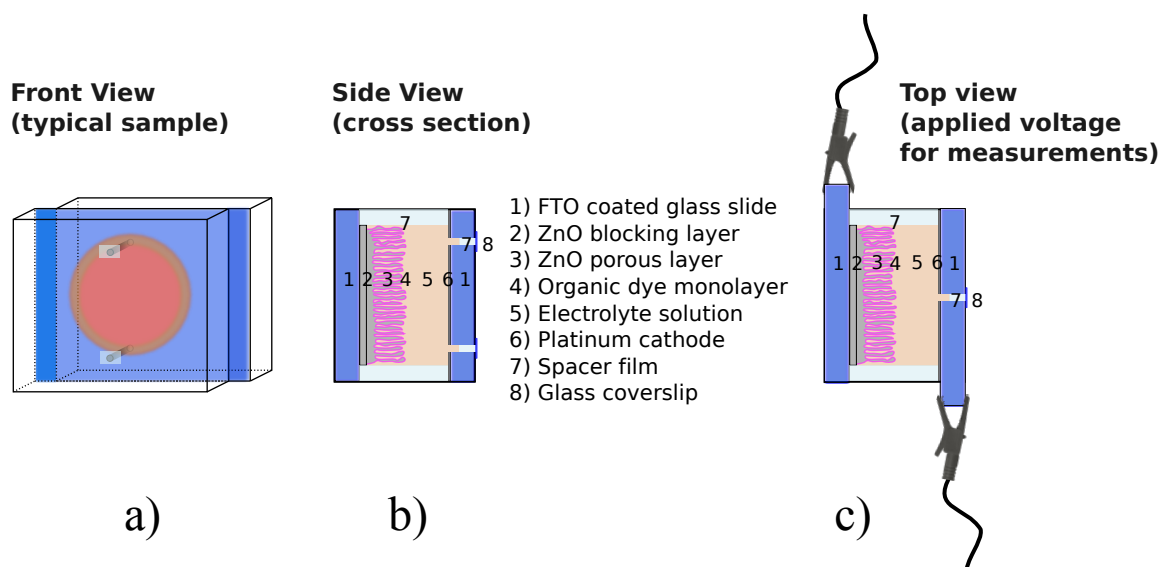


Figure 2.4: Diagrams of an organic-DSSC sandwich cell sample showing the front view (panel a), the side view depicting all the components (panel b) and a typical way in which electrodes are contacted for measurements, top view (panel c).

optimise the optical density of the cells for transient absorption spectroscopy measurements done through transmission. Details of how the cells were made will be given later on.

The Organic Dyes Used

As mentioned, the most commonly used organic dye with ZnO in DSSCs is the indoline dye D149. Although the dye is known to produce high cell efficiencies, it only remains adsorbed to the ZnO surface for a few weeks, after which it desorbs and is present in the electrolyte solution. When photoexcited in solution, it is no longer able to inject electrons into the conduction band of the semiconductor. The overall efficiency of the DSSC drops and the cells are of no further use. To increase the lifetime of indoline dye sensitised solar cells, D149 dye derivatives were developed by replacing the ethyl group of D149 with a longer alkyl chain and a second carboxyl anchor. Through the addition of the second anchor group, the lifetime of the DSSCs was improved drastically from a few weeks to longer than a year without compromising their efficiency [26].

The alkyl chain onto which the second carboxyl anchor group is bonded, can be synthesised of varied length. The indoline dyes DN285, DN216 and DN91 are derivatives of D149 with varying alkyl chain length of the second anchor group. The chemical structures of all the organic dyes mentioned above and used in this work can be seen in figure 2.5. Fully operational DSSC samples were sensitised with one of the three double anchor dyes. Both macroscopic and microscopic measurements were then carried out to determine the effect of the alkyl chain length on the fully functioning DSSC.

Measurements Taken on DSSCs

Macroscopic measurements enable us to determine parameters such as the maximum current and voltage produced by the solar cell as well as its efficiency. From these measurements, such as I-V curves, we are then able to determine which of the aforementioned indoline dyes behave more efficiently within the same system. However, to observe the charge dynamics in real time within the DSSC an ultrafast microscopic method must be employed as these

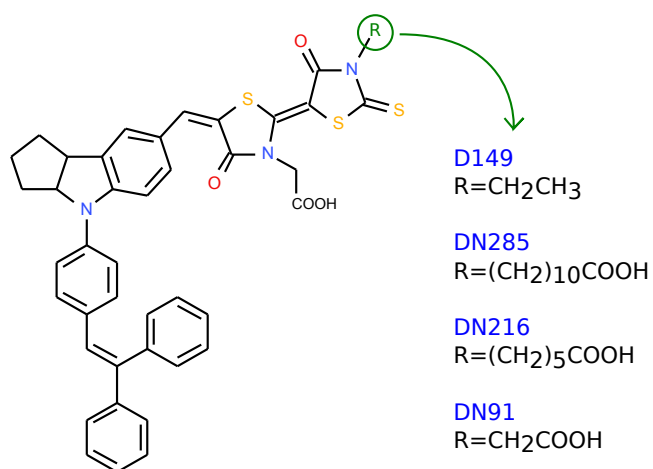


Figure 2.5: Schematic of the indoline dye D149 and its double anchor derivatives, DN285, DN216 and DN91.

processes occur on femtosecond to picosecond time scales. With the use of ultrafast transient absorption spectroscopy we are able to determine the lifetime of the electron transfer from the dye to the semiconductor. In addition, the lifetimes of the oxidised dye molecule as well as the ground state bleaching of the dye are also determined.

3. Preparation of DSSCs

3.1 Electrodeposition of ZnO

As mentioned previously, one of the advantages of using ZnO over TiO₂ as the semiconductor in DSSCs is that a ZnO thin film can be electrodeposited at a low temperature of 70°C. In contrast, TiO₂ thin films are made using the Sol-gel method and sintered at the high temperature of 450°C. The electrodeposition of ZnO thin films is cost effective, simple and reproducible. The solar cell samples made and studied in this work were produced according to the well established method of Yoshida *et al* and Ichinose *et al*, for details please refer to appendix A [24; 27].

Although mechanically flexible substrates such as plastic or various fibres could have been used for deposition of the ZnO, FTO coated glass slides were chosen. The glass slides are mechanically rigid and transparent therefore ensuring that the DSSC samples made could be measured using ultrafast transient absorption spectroscopy. A circular area with radius 1 cm was marked off on the glass slide using a strong adhesive masking tape. This way only the $\pi \text{ cm}^2$ area cut out of the tape was exposed to the electrodeposition bath and the shape and size of the ZnO thin film was therefore controlled.

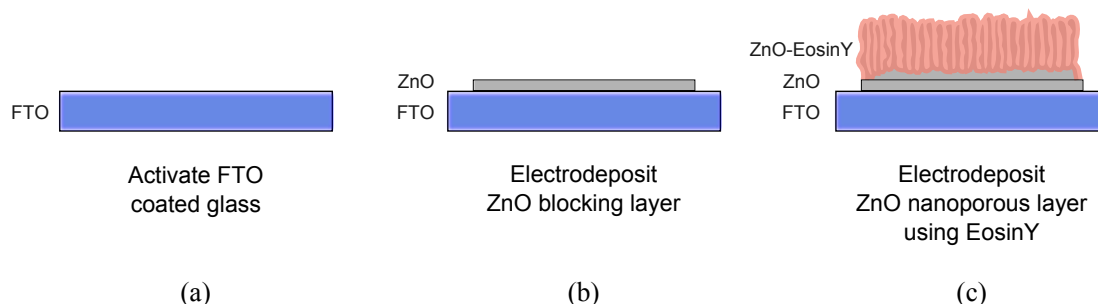


Figure 3.1: Schematic of the FTO coated glass slide after activation (panel a), showing the electrodeposition of the ZnO blocking layer (panel b) and the electrodeposition of a ZnO nano-porous structure with EosinY (panel c).

The electrodeposition process starts with the activation of the FTO on the glass slide as can be seen in figure 3.1 panel (a). This is necessary as it increases the number of sites onto which the ZnO crystals can grow. Through this process, we ensure that the ZnO thin film will be compact, transparent and highly orientated. The next step is shown in panel (b) and it is the electrodeposition of a ZnO blocking layer onto the activated FTO. The blocking layer is a tightly packed ZnO thin film that serves as a boundary to stop the back transfer of electrons from the FTO to the electrolyte. In this way we avoid internal short circuiting of the cell. This layer is deposited to a thickness of approximately $1 \mu\text{m}$ by adjusting the deposition parameters [28]. Finally, to build the highly nanoporous ZnO, the dye EosinY is used in the electrodeposition bath as a structure directing agent. The presence of the EosinY dye causes the ZnO to crystallise around it and build up a network of pores as shown in panel (c). The thickness of this porous ZnO layer is approximately $5 \mu\text{m}$ and the pore size is approximately 10 nm as it is determined by the average EosinY agglomerate size. The structure of the nanoparticle ZnO thin film can be seen in figure 3.2.

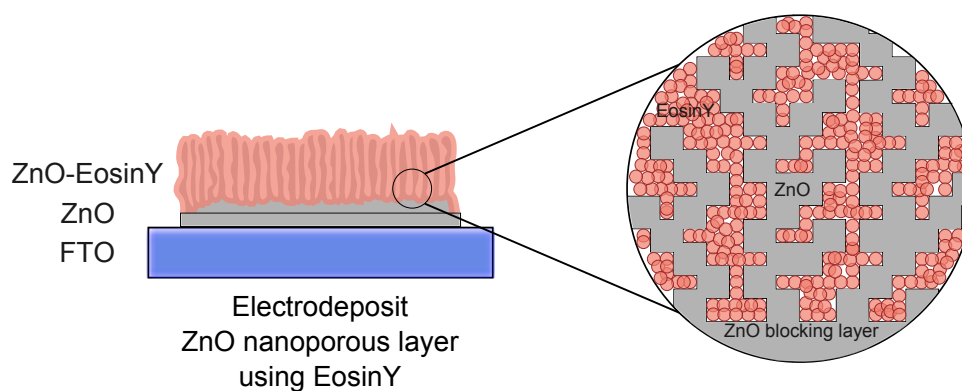


Figure 3.2: Detailed representation of the highly porous nanoparticle ZnO thin film electrodeposited with the use of the structure directing agent EosinY.

3.2 Adsorption of Organic Dye

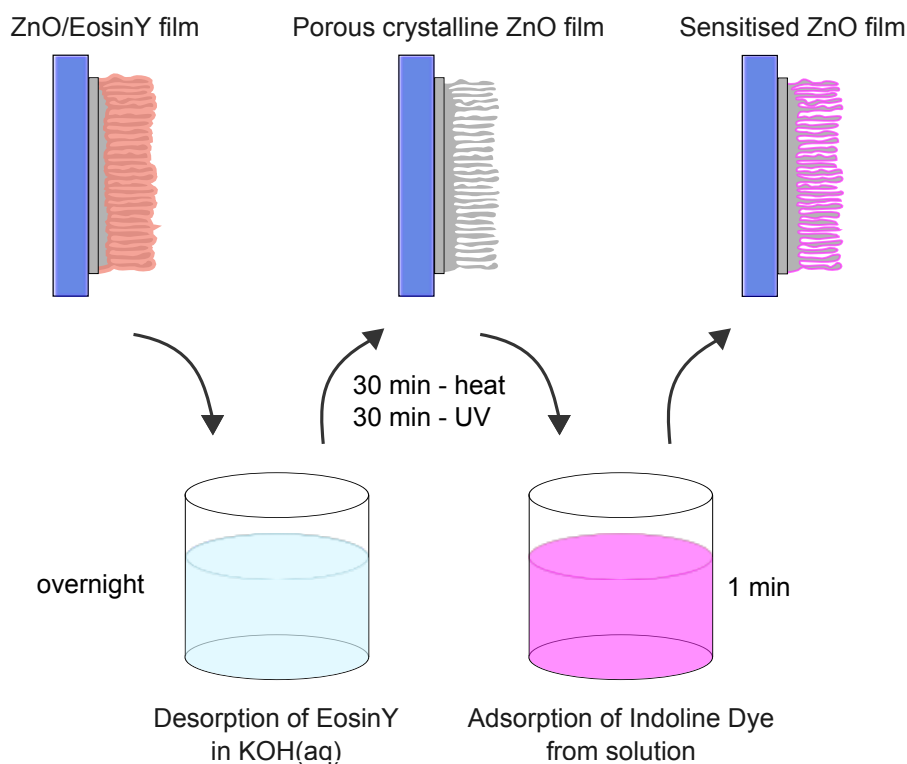


Figure 3.3: Process used to desorb the EosinY from the ZnO thin film, prepare the film and sensitise it with an indoline dye from solution.

Desorption of EosinY

As can be seen in figure 3.3, before the organic indoline dye can be deposited on the ZnO thin film, the EosinY must be desorbed. This is done by submerging the glass slide in a

KOH aqueous solution overnight. The strong base etches the EosinY molecules away from the surface of the ZnO nanoporous structure. Furthermore, because the process is carried out in the presence of natural sunlight, the ZnO acts as a photocatalyst to destroy the EosinY molecules. This process leaves the ZnO thin film bare and ready to be prepared for sensitisation with an organic indoline dye. As all the EosinY molecules are accessible to the KOH solution, this serves as an indication that there are no closed ZnO cavities present, therefore allowing a maximum area for sensitisation with the indoline dye.

Preparation of the ZnO Thin Film for Sensitisation

The ZnO thin film is prepared for dye loading through two processes as shown in figure 3.3. First it is heated on a heating plate at 130°C for 30 minutes. Through heating, any remaining water evaporates from within the ZnO pores. Additionally, any remaining ZnOH from the desorption process is converted to ZnO. The film is then placed under a UV lamp for 30 minutes. During this step, OH groups are created on the surface of the ZnO structure. They are used to aid the adsorption of the indoline dye, as the carboxyl anchor groups bond to the ZnO surface [29].

Adsorption of the Indoline Dye

Finally, the indoline dye is sensitised onto the ZnO surface as per Figure 3.3. This is done by submerging the entire glass slide into a blacked out Petri dish filled with dye solution for a given time. Samples were made with each of the three indoline dyes mentioned previously, DN285, DN216 and DN91. They are derivatives of the organic dye D149 with a second carboxyl anchor group to help adsorb onto the surface of the ZnO. The only difference between the three dyes is the alkyl chain length onto which the second carboxyl anchor is bonded. The three dyes not only look very similar (dark pink in solution) but have very similar chemical properties.

The optimal dye loading time for the ZnO nanoporous structure to be covered with an even monolayer and no unwanted dye aggregates to form is 10 minutes [30]. However, a dye loading time of 1 minute was used to ensure that the samples were not too light-scattering for ultrafast transient absorption spectroscopic measurements. By doing this, the overall efficiencies of the cells were reduced, but the charge dynamics within the DSSCs remained unaffected. A photograph of a π cm² ZnO thin film sensitised with the indoline dye DN91 can be seen in figure 3.4. This is the working electrode of the dye sensitised solar cell.

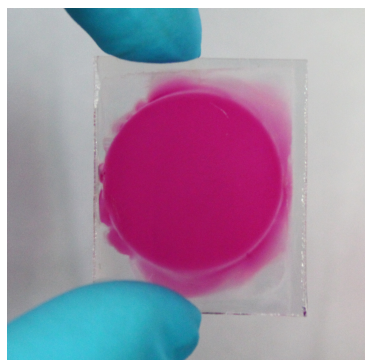


Figure 3.4: Photograph taken of a 1 cm diameter DN91 sensitised ZnO thin film electrodeposited on a FTO coated glass substrate.

In the same way, a number of photoanodes were prepared, each sensitised with one of the three dyes. They were then used to build fully functioning DSSCs.

3.3 Building the Solar Cell

In addition to the working electrode, every DSSC must have a counter electrode. To make the counter electrodes we used FTO coated glass slides. Two holes were drilled in each of these glass slides. The positions of the two holes were chosen to line up within the working electrode

parameters upon building the cell. The conductive side of the glass was sputter-deposited with Pt by adding two drops of 5 mM ethanoic solution of hexachloroplatinic acid and heating the slides at 450°C for 30 minutes. As mentioned previously the Pt layer (approximately 50 nm thick) acts as a catalyst to faster reduce the redox couple at the cathode.

To build the cell, a piece of spacer film was cut approximately 5 mm shorter than the length of the glass slides. A hole was then stamped out of the film equal to the size of the working electrode. For the solar cell samples made for these measurements a $\pi \text{ cm}^2$ area was cut out. The film was then sandwiched between the two electrodes and the cell placed on a heating plate warmed to 130°C. The spacer film melts at 120°C so the cell was sealed using a flat-tip soldering iron set to 230°C and applying the additional heat and pressure from the top as per figure 3.5.

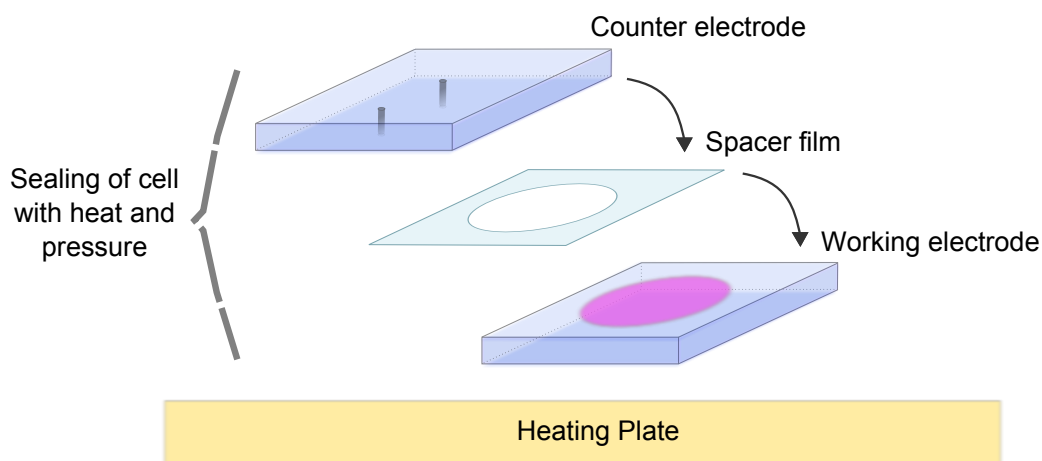


Figure 3.5: Sealing of the DSSC using spacer film, heat and pressure.

Once the cell was sealed, the electrolyte solution containing the iodide/triiodide redox couple was added through one of the drilled holes, see figure 3.6. The holes were covered using two small glass coverslips and sealed using spacer film, pressure and heat once again. As an example, figure 3.7 is a photograph of a fully functioning DSSC built using the method described above.

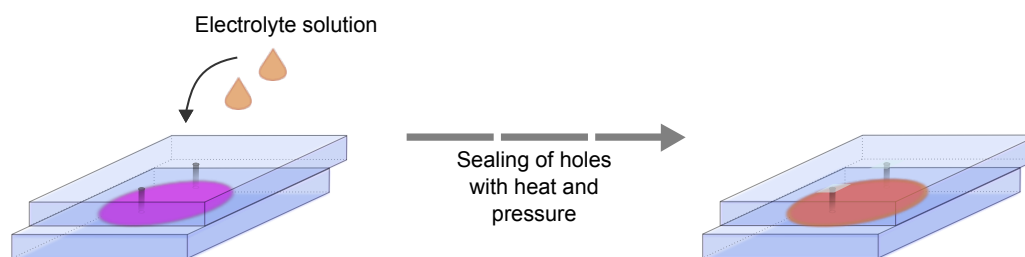


Figure 3.6: Adding the electrolyte solution and sealing the two drilled holes using spacer film, pressure and heat from above.

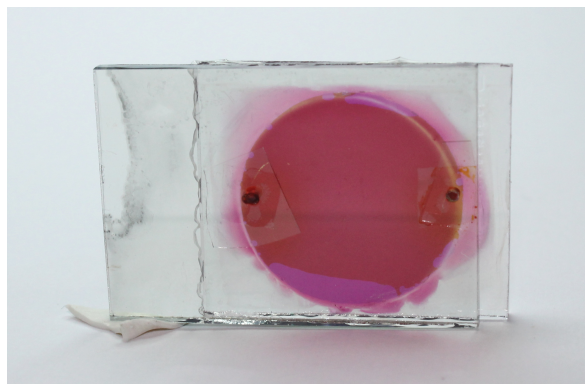


Figure 3.7: Photograph taken of a fully functioning DN91 sensitised solar cell prepared using the method described here.

3.4 Photoelectrochemical Characterisation

One of the most useful ways of characterising a working DSSC is through its I-V curve. A solar cell can be compared to a diode under illumination, see figure 3.8. The series resistance is caused by the resistance present in the materials such as the FTO and the cables used to connect the cell to an external voltage supply for the I-V curve measurements. On the other hand, the shunt resistance describes the recombination within the DSSC [31; 32].

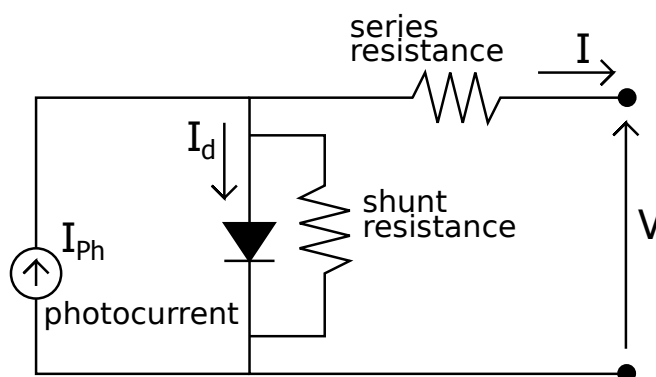


Figure 3.8: Diode model used to describe a dye sensitised solar cell.

Introduction to I-V Curves of DSSCs

A dye sensitised solar cell shows the characteristic I-V curve of a diode shifted to higher negative currents as the light intensity increases and the cell generates power. As is convention, the current axis is inverted and the I-V curve of a solar cell has the form shown in figure 3.9. A number of properties can be learnt from the I-V curve of a solar cell [33]. The current axis intercept is the maximum current that the solar cell can produce – the short circuit current density (J_{SC}). The voltage axis intercept is the maximum voltage supplied by the cell – the open circuit voltage (V_{OC}). The open circuit voltage depends only on the separation between the quasi-Fermi level of the ZnO and the redox potential in the electrolyte as was shown and described in the previous chapter. Therefore the dye used should only affect the J_{SC} and not the V_{OC} , assuming that they are of very similar acidity. Furthermore, the short circuit current depends on the cell area. To be able to compare cells of different surface areas, it is better to

plot the photocurrent density. All the DSSC samples made in this work were measured out with a stamp of $\pi \text{ cm}^2$ area and sensitised for the same duration. Converting to photocurrent density, in this case, is simply a formality. During the I-V curve measurements, the lamp intensity and its spectrum were kept constant.

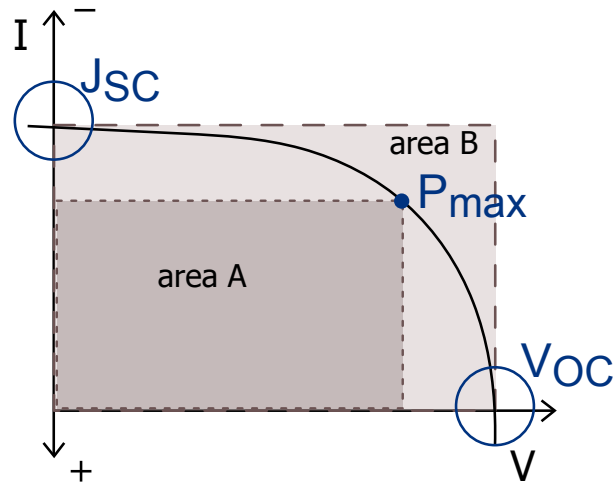


Figure 3.9: A sketch of an I-V curve showing the short circuit current, open circuit voltage, maximum power and areas used for the calculation of the fill factor.

Even though the J_{SC} and V_{OC} are the maximum current and voltage produced by the cell, the power is zero at both of these points. To determine the maximum power, P_{max} , the fill factor (ff) is used in conjunction with the short circuit current and open circuit voltage as

$$P_{max} = ff (J_{SC} \cdot V_{OC}). \quad (3.4.1)$$

The fill factor holds values between 0 and 1, and is defined as the ratio of the maximum power producible by the cell to the product of the J_{SC} and the V_{OC} . As can be seen in figure 3.9 it can be calculated graphically by the ratio of the largest rectangle which fits under the curve (area A) determined by P_{max} , to the rectangle created by intercepting the J_{SC} and V_{OC} values (area B)

$$ff = \frac{\text{areaA}}{\text{areaB}}. \quad (3.4.2)$$

Therefore a very rounded I-V curve produces a low fill factor. The roundness of the I-V curve is a representation of the internal resistance within the DSSC. The slope of the curve at the short circuit current describes the shunt resistance within the cell, and the slope of the curve at the open circuit voltage is a representation of the series resistance within the cell [31]. Total solar-to-electrical energy conversion efficiency (η) is the most commonly used parameter to compare solar cells and it is defined as the ratio of energy output from the solar cell to input energy from the sun

$$\eta = \frac{P_{max}}{P_{in}} = \frac{J_{SC} \cdot V_{OC} \cdot ff}{P_{in}}. \quad (3.4.3)$$

Therefore a high fill factor, J_{SC} and V_{OC} results in a high cell efficiency [1].

I-V Curve Measurements on our cells

Figure 3.10 shows three representative light I-V curves taken for DSSC samples made in the same way. Each of the samples was sensitised with one of the indoline dyes DN91 (black), DN216 (red) and DN285 (blue). If we compare the three types of samples measured, we can see that the open circuit voltage is very similar. This is expected as the V_{OC} is the maximum voltage available from the solar cell and it is determined by the potential difference between the Fermi level energy of the ZnO and the iodide/triiodide redox potential. It is therefore not depended on the dye used, and only on the ZnO thin film and electrolyte solution. As these two parameters and intensity of light source (1 sun) were kept constant for all the solar cells, the V_{OC} was also constant (~ 0.6 V) for all the samples indicating a high reproducibility of the solar cell samples.

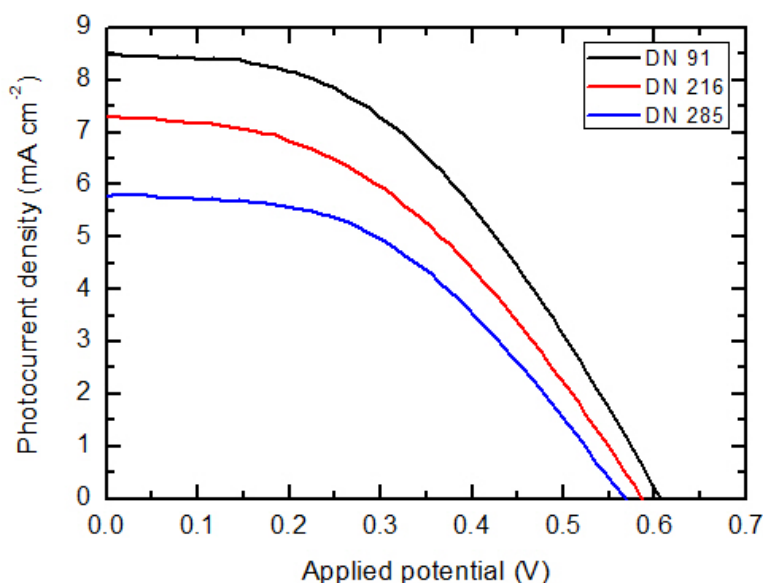


Figure 3.10: Three representative light I-V curves of samples made in the same way each sensitised for 1 minute with one of three indoline dyes, DN91 (black), DN216 (red), DN285 (blue).

The short circuit current of each of the samples in figure 3.10 however differs from one another. It is highest for the DSSC samples sensitised with DN91, the indoline dye with the one carbon alkyl chain to the second anchor group, and lowest for the samples sensitised with DN285, the dye with the ten carbon alkyl chain to the second anchor group. Therefore the J_{SC} decreases with increasing alkyl chain length as $J_{SC}(DN91) > J_{SC}(DN216) > J_{SC}(DN285)$. Additionally, the fill factors of the cells are approximately the same for all three cells shown: $ff(DN91) = 0.45$, $ff(DN216) = 0.43$ and $ff(DN285) = 0.46$.

The I-V curves of solar cells sensitised with D149 are not presented here as the samples made previously with D149 are not comparable, although the new dyes containing two carboxyl anchors will be compared to D149 throughout this work.

The higher short circuit current measured for the samples sensitised with DN91 could have been caused for a number of reasons. The DN91 dye could have a faster electron injection time from its lowest unoccupied molecular orbital into the conduction band of the ZnO and therefore a higher injection yield compared to loss processes such as intramolecular relaxation [34]. In contrast, the light-harvesting efficiency might be responsible for the higher short circuit current of the DN91 sensitised solar cells. In this case the dye molecules arrange themselves

more efficiently on the ZnO surface, so more molecules per area could be deposited during the 1 minute dye loading time in comparison to DN216 and DN285. Additionally, the difference between the J_{SCS} measured could be a combination of these two reasons.

To determine the cause of the difference in the measured J_{SCS} for the DSSC samples, the number of dye molecules per area for a cell could be calculated for the three different dyes using their extinction coefficients and steady state spectra. However it requires us to assume that there is no contribution from the ZnO in the visible range and it provides no information on the orientation of the different dye molecules on the ZnO surface, therefore no additional information about the electronic coupling between LUMO of dye to conduction band of ZnO. Therefore we rather focus our attention on explaining the spectroscopic characteristics of the dyes and the molecular processes which occur in dye sensitised solar cells. The lifetimes and probability amplitudes of these processes were measured with the use of pump-probe ultrafast transient absorption spectroscopy for the samples loaded with the three different dyes and compared in the following chapters.

4. Femtosecond Transient Absorption Spectroscopy

4.1 A Typical Spectrum

All the experiments were carried out with the use of ultrafast transient absorption spectroscopy. This method allows us to observe the change over time in the absorption spectrum of a photoexcited molecule or solid. The change is proportional to the population of molecular states (ground and excited) or valence and conduction bands in solids respectively. Therefore molecular dynamics and charge dynamics between molecules and solids can be observed. All we have to do is monitor the absorption spectrum of our system as it evolves in time.

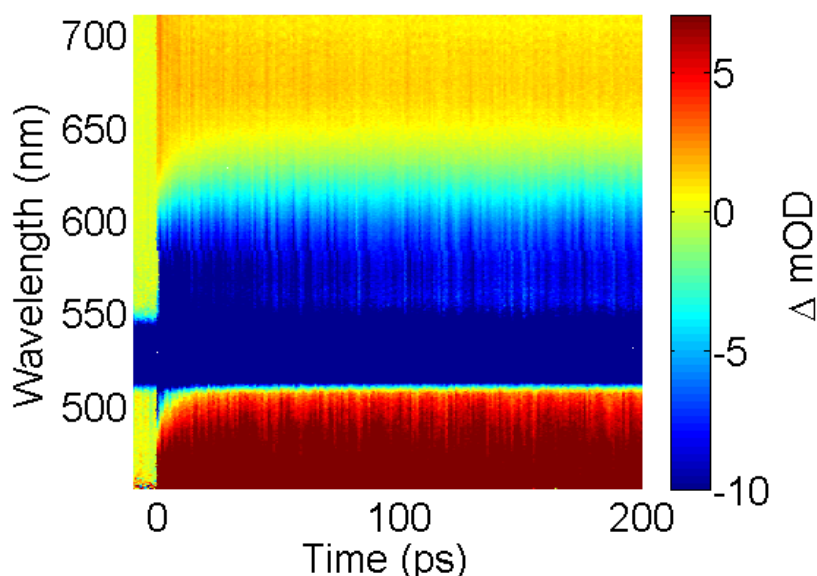


Figure 4.1: A long time window transient absorption spectrum taken of a fully operational DSSC sensitised with the indoline dye DN216 (pumped with a pulse of central wavelength of 530 nm and probed with a white light continuum).

A typical transient absorption spectrum is shown in figure 4.1. It was taken on a fully functioning DSSC sample using the pump-probe femtosecond transient spectroscopic measurement technique. The wavelength is plotted on the y-axis, the time on the x-axis and the change in optical density (ΔOD) using a colour map on the z-axis. The ΔOD value for each wavelength and time is a ratio of the absorption spectrum of a molecule's excited state to its absorption spectrum in the ground state which increases the sensitivity of the experiment. With the use of the Beer-Lambert law, the optical density or absorbance at a given wavelength can be described as in equation 4.1.1

$$OD(\lambda) = -\log \left\{ \frac{I(\lambda)}{I_0(\lambda)} \right\} = \epsilon_{\text{mol}}(\lambda) \cdot c \cdot l, \quad (4.1.1)$$

where $OD(\lambda)$ is the wavelength dependent optical density which is also referred to as the absorbance of a particular sample. It is defined as the product of the molar extinction

coefficient $\epsilon_{\text{mol}}(\lambda)$, the concentration of the sample c and the thickness of the sample l . $I(\lambda)$ is the measured light intensity transmitted by the sample and $I_0(\lambda)$ is the reference transmitted light intensity.

Using the colour map chosen as in figure 4.1, both negative and positive changes in optical density can be observed. Blue indicates more light transmission measured by the detector (negative ΔOD values). This can be due to a lower population of the initial state – a process named bleaching.

Additionally, it can also be caused through stimulated emission out of an excited state, where the probe beam provides the stimulating photon. In this way fluorescence can be detected. The relaxation of a photoexcited electron from the LUMO back to the HOMO is accompanied by a fluorescence signal. The fluorescence yield is dependent on the relative number of electrons relaxing back to the ground state. For an indoline dye in solution, the fluorescence yield is high as the excited molecules couple to their environment well. In our situation, the dye molecules are attached to the ZnO semiconductor which quenches the fluorescence. Therefore a fluorescence signal is not observed in the transient spectra of solid state samples where the dye is adsorbed to the semiconductor.

A positive change in optical density is shown in red. This indicates less light transmission measured by the detector and it is due to a higher population of newly generated states. A ΔOD equal to zero is shown in green. It is representative of no change between the absorption spectrum of the excited dye molecules and the absorption spectrum of the dye molecules in the ground state, as can be seen before time t_0 . At time t_0 both the pump and probe pulses are simultaneously interacting with the sample and the charge dynamics are started, see below.

Therefore in a transient absorption spectrum, a change in population of molecular states can be observed for the dye molecules in both their neutral and oxidised forms.

What can be Learnt from a Transient Spectrum

To be able to understand a transient absorption spectrum, we must look closer at the processes within the DSSC which affect the electron populations of the various states. See a simplified version of the charge transfer processes within a DSSC in figure 4.2. The photoexcitation process marked 1 is achieved using a laser pulse of correct wavelength to provide adequate energy. This is called the pump pulse and is usually set to the wavelength corresponding to an absorption maximum of the dye. If the sample is probed before the photoexcitation has taken place, there is no change in optical density due to the pump pulse. Therefore the area of the transient absorption spectrum of figure 4.1 before the sample has been pumped is green ($\Delta\text{OD} = 0$). Probing refers to the measurement of the absorption spectrum of a sample as a function of time.

In general, transitions to any states, photoinduced ions, spontaneous fluorescence and Raman signals can all be observed as changes in the transmitted spectrum of a sample as a function of time. Although the samples in this work are probed with visible light, the probe beam can also be x-rays or electrons which are diffracted.

The constant blue saturated signal at a central wavelength of 530 nm occurring throughout the transient spectrum is due to the pump pulse scattering off the solid state sample and the detector measuring an increase in light transmission at that wavelength.

If the sample is probed after the photoexcitation process, a number of signals can be observed in the visible wavelength range and assigned to processes within the DSSC as shown in figure 4.3. The blue signal at 550 nm can be assigned to the wing of the ground state bleaching (GSB) signal. After the photoexcitation process, the dye molecules are in their excited state and the population of electrons in the HOMO of the dye is greatly reduced, here by 2%, therefore causing an increase in light transmission measured by the detector. The GSB

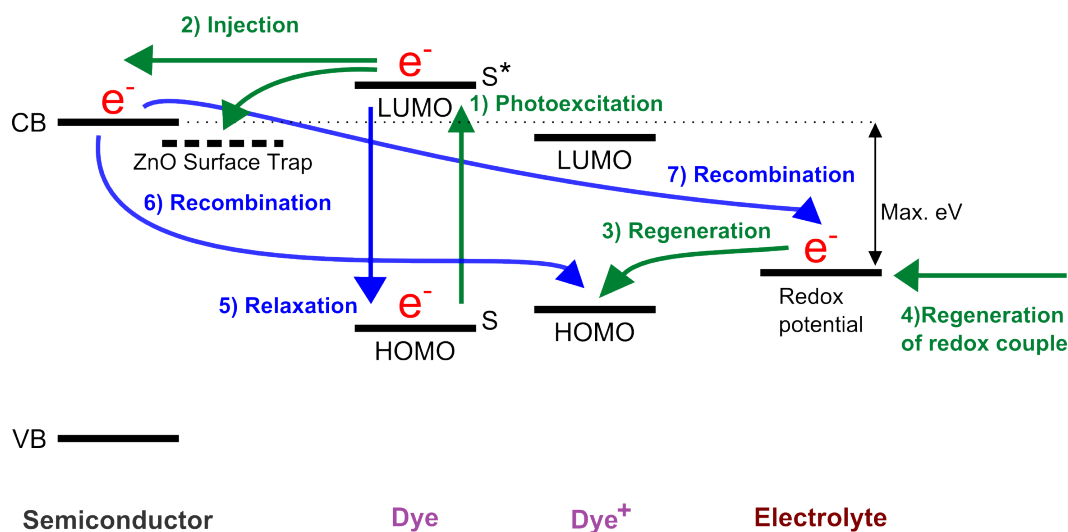


Figure 4.2: A schematic of photoinduced charge transfer processes which occur within a DSSC.

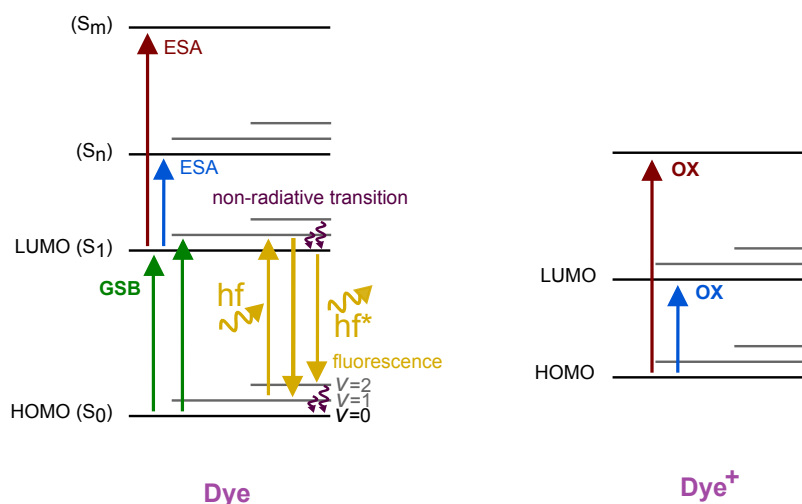


Figure 4.3: Jablonski diagrams depicting the signals which can be observed in a transient absorption spectrum.

signal decays back to zero with time as the ground state of the dye molecules is repopulated through processes marked 3, 5 and 6 in figure 4.2.

The electrons which have been excited through photoexcitation increase the population of the LUMO of the dye. They can therefore be further excited to higher energy levels when the sample is probed as can be seen in figure 4.3. This process is called excited state absorption (ESA) and due to a decrease in light transmission measured by the detector, it causes a red signal. The red ESA signals can be seen at central wavelengths of approximately 675 nm and 480 nm. They decay back to zero through processes 2 and 5 in figure 4.2 and are short-lived as they depend on the ultrafast injection time.

Unfortunately the two absorption maxima of the oxidised form of the dye (OX) are also at central wavelengths of approximately 675 nm and 480 nm. The dye is oxidised through the injection of electrons into the conduction band of the ZnO. Therefore when the sample is probed, the electrons in the HOMO of the oxidised dye molecules can be excited to higher energy levels as shown in figure 4.3. As less light transmission is detected, the OX signals are red in the transient spectrum of figure 4.1. They decay back to zero through processes 3 and

6 in figure 4.2 and are therefore longer-lived than the ESA signals as they do not depend on the ultrafast injection time. The overlapping ESA and OX signals can be separated as they decay on different time scales.

How a Transient Absorption Spectrum is Taken

A transient absorption spectrum is taken by measuring the change in optical density versus wavelength for each time step shown in figure 4.1. For better results, we average over 3000 change in absorption measurements for each time step. As the charge dynamics in the solar cell occur on the femtosecond and picosecond time scales, we are not able to detect the evolution of the GSB, ESA and OX signals in real time with even the fastest electronics. To overcome this physical limit, pump-probe spectroscopy is used.

4.2 Pump-Probe Spectroscopy

Femtosecond pump-probe spectroscopy is achieved with the use of two ultrashort laser pulses split from the same laser pulse – the pump pulse and the probe pulse. The spectrum of the pump pulse is adjusted with the use of a non-linear optical parametric amplifier (NOPA) to correspond to the excitation energy of the molecule that is being studied. The spectrum of the probe pulse is either generated in a sapphire crystal as a white light (WL) spectrum, or selected with the use of a NOPA to probe a certain wavelength region.

The duration of a pulse generated with the use of a NOPA is less than 50 fs, while the chirp corrected (see below) white light pulse is approximately 150 fs. Therefore the resolution of a NOPA pump - WL probe transient absorption spectrum is less than 200 fs, and the resolution of a NOPA pump - NOPA probe transient spectrum is better than 100 fs. NOPA - WL measurements are usually taken first in order to get an overview of the entire visible spectrum. To better resolve the ultrafast signals seen in the NOPA - WL transient spectra, NOPA - NOPA measurements are then taken on the same sample.

Experimental Method

The pump pulse photoexcites electrons from the HOMO to the LUMO of the dye therefore exciting the molecules from their ground state to their excited state. This process is shown in figure 4.4 together with the respective electron densities calculated with density functional theory (DFT) for the ground and excited states of the indoline dye D149 [19]. The probe pulse arriving after the pump pulse then probes the absorption of excited molecules as well as molecules still in the ground state.

To be able to determine the dynamics of a molecule, this process is repeated for different time intervals (Δt) between the arrival of the pump and probe pulses at the sample. Therefore as can be seen in figure 4.4, if the pump pulse interacts with the sample at time t_0 and the probe pulse at time t_i , consecutive spectra are then collected by varying Δt . For experimental reasons (see section 4.2), it is better to keep t_i fixed and vary t_0 . This is done with the use of a mechanical delay stage. The mechanical delay stage simply varies the distance which the pump pulse travels, therefore varying the time (t_0) at which it arrives at the sample, refer to figure 4.5. Distance l and time t are related with the speed of light c as $l = c \cdot t$, so $1 \mu\text{m} \cong 3.3\text{fs}$. Moving the translation stage $1 \mu\text{m}$ results in a time delay of 6.6 fs as the stage is set up in reflection, see figure 4.7.

However, by looking at the Beer-Lambert law of equation 4.1.1, it can be seen that in order to determine the absorption spectrum of the dye molecule from the transmitted spectrum of the probe pulse, the spectrum of the probe pulse must be known. Measuring the spectrum of the probe pulse consistently for each shot has not been realised experimentally in our lab.

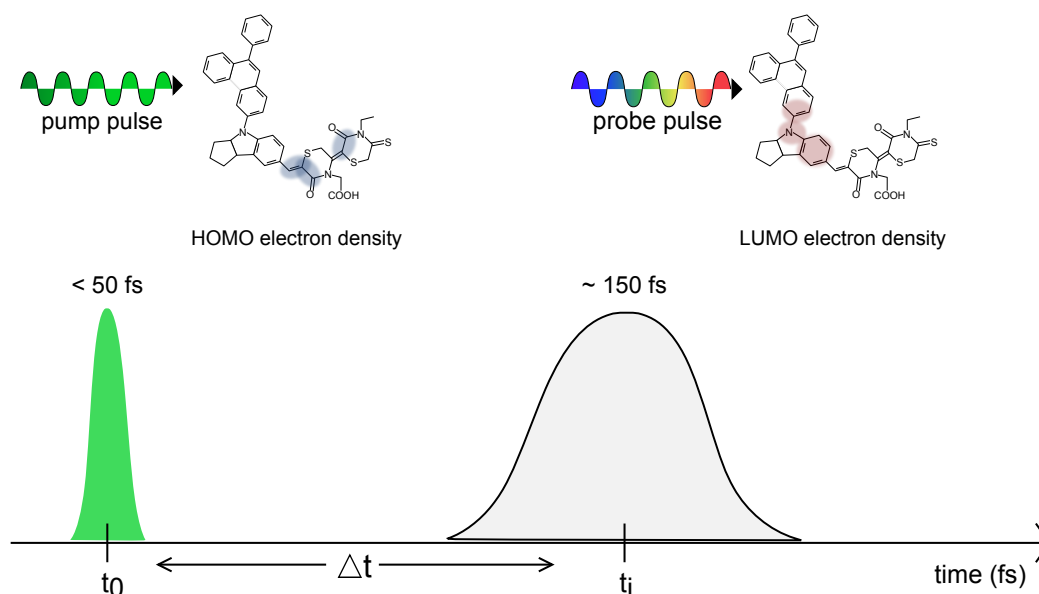


Figure 4.4: The pump pulse excites the dye in the sample from its ground state to its excited state at time t_0 . The probe pulse arrives at time t_i and probes the sample containing the excited molecules. The difference in time between the pump pulse and the probe pulse is denoted as Δt .

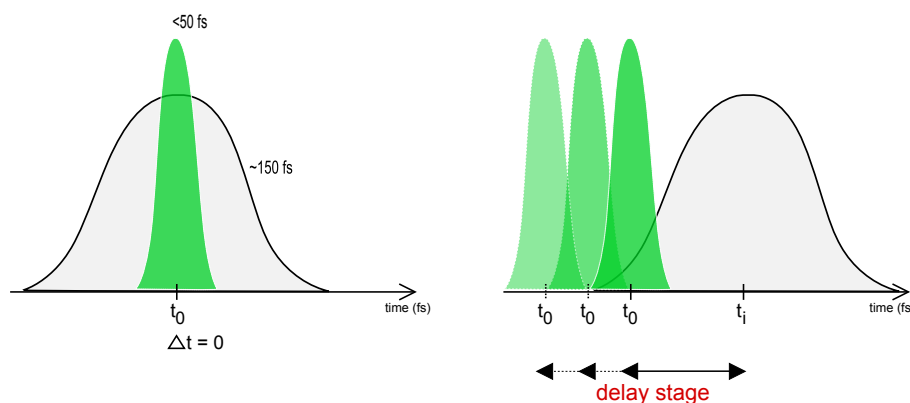


Figure 4.5: The arrival of the pump pulse at the sample is varied with respect to the probe pulse by varying the distance it travels so that spectra can be stored for each time step of a transient absorption spectrum.

Therefore a chopper was introduced into the pump beam to block out every second pump pulse. In this way, every second shot, an unexcited (unpumped) sample is probed and a reference spectrum obtained. See figure 4.6.

The spectrum obtained from probing a pumped sample (pumped spectrum) is then divided by the reference spectrum (unpumped spectrum) that follows it to obtain a change in optical density as a function of wavelength ($\Delta OD(\lambda)$). By doing this, the spectrum of the probe pulse is no longer necessary to observe changes in optical density over time, see equation 4.2.1: $I_P(\lambda)$ is the measured wavelength dependent transmitted light intensity for the pumped spectrum, $I_{UP}(\lambda)$ is the measured wavelength dependent transmitted light intensity for the unpumped spectrum, and $I_W(\lambda)$ is the measured wavelength dependent light intensity of the probe pulse spectrum – either white light, or light generated in a NOPA,

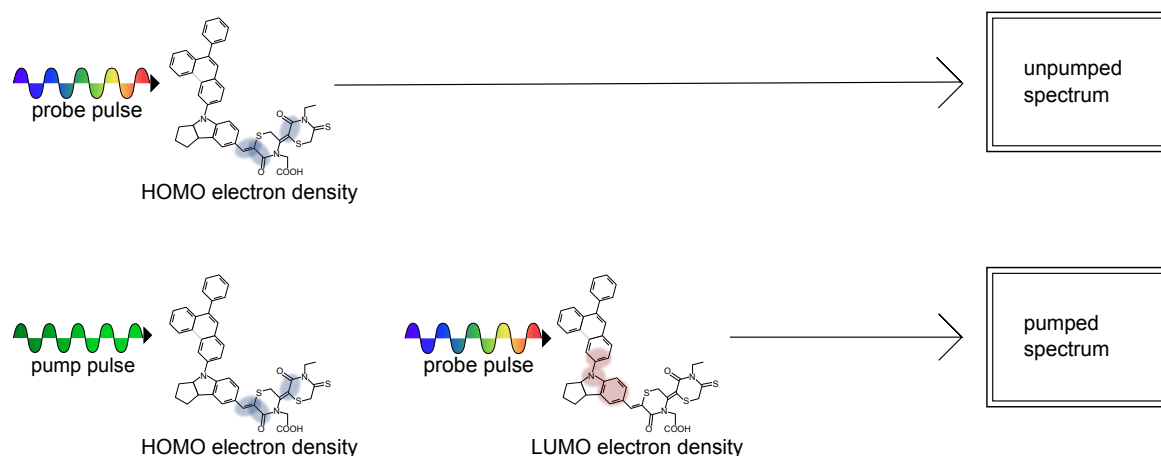


Figure 4.6: Through probing the sample, both a pumped and an unpumped spectrum is obtained as every second pump pulse is chopped.

$$\begin{aligned} \frac{I_P}{I_W} \cdot \frac{I_W}{I_{UP}} &= 10^{-OD_P} \cdot 10^{+OD_{UP}}, \\ &= 10^{-(OD_P - OD_{UP})}, \\ \frac{I_P}{I_{UP}} &= 10^{-\Delta OD}. \end{aligned} \quad (4.2.1)$$

By measuring the ratio of pumped to unpumped spectra for each time step and using the mechanical translation stage to change the time delay between the pump and probe pulses at the sample, we are able to build up a transient absorption spectrum of ΔOD values for each probe wavelength and time step, as we have seen in figure 4.1.

Experimental Setup

The experimental setup used for femtosecond pump-probe spectroscopy is depicted in figure 4.7 [35]. The femtosecond laser is designed as a chirped pulse amplifier (CPA) with the use of a femtosecond oscillator (fibre laser) and a Ti:Sapphire amplifier to produce pulses of 150 fs at a central wavelength of 775 nm with a repetition rate of 1 kHz.

As can be seen in figure 4.7, the CPA pulse is split into two along two separate pathways with the use of a 50:50 beam splitter. Along path 1 the pulse is led into a NOPA therefore allowing us to tune the central wavelength of the pulse between 470 nm and 700 nm. The output pulse is then compressed using a prism compressor to sub 50 fs and is used as the pump pulse. The pulse split along path 2 is used as the probe pulse – either a white light pulse or another NOPA pulse. For a white light probe pulse, the fundamental pulse (775 nm) is converted to a white light continuum with the use of a sapphire crystal through a process named white light generation (WLG). Ultrashort pulses with a spectrum spanning from approximately 450 nm to the near infra-red are generated through WLG, see below. A NOPA probe pulse is generated in the same way as the pump pulse and also compressed with the use of a prism compressor to sub 50 fs.

The mechanical delay stage in figure 4.7 is placed in the beam path of the pump pulse. This is done as the NOPA pulse is much more stable than the white light continuum. With the use of the delay stage the distance which the pump pulse travels before it reaches the sample can be varied and therefore the time (t_0) at which it arrives at the sample can be changed. In this way the time between the arrival of the pump and probe pulses at the sample

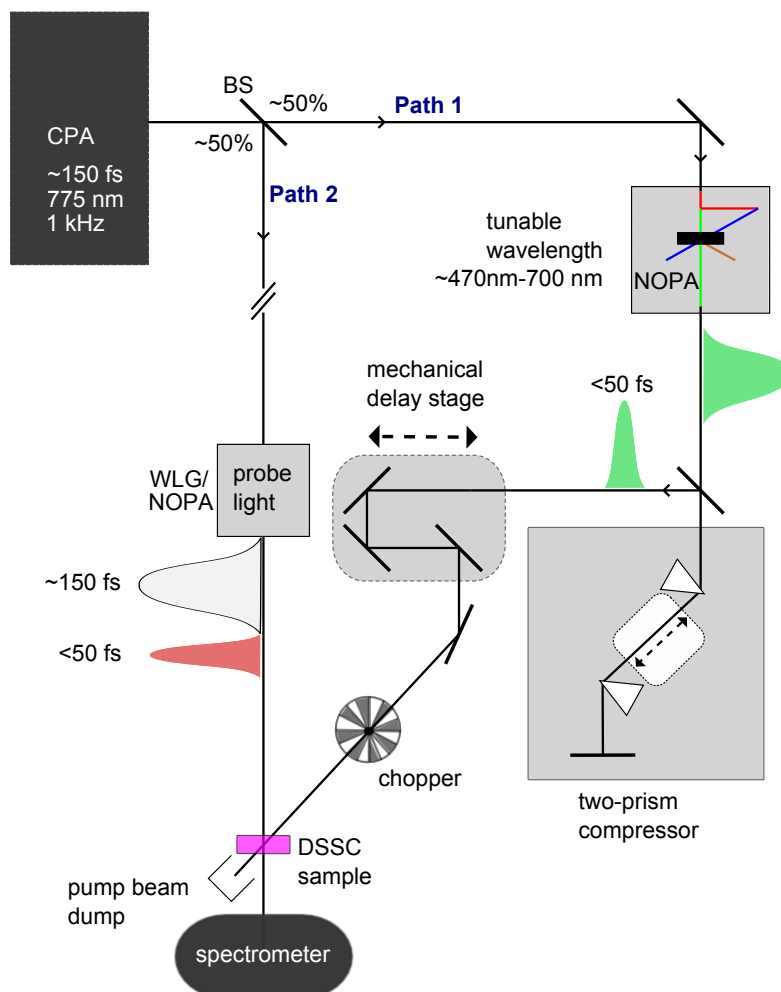


Figure 4.7: The pump-probe experimental setup used to carry out transient absorption spectroscopy. The figure shows a laser pulse split along two paths, path 1 used to generate the pump pulse and path 2 used to generate the probe pulse.

(Δt) can be varied. The accuracy of the delay stage is $2 \mu\text{m}$. With the use of $t = \frac{l}{c}$ where t is time, l distance and c the speed of light, this translates to an accuracy of 13 fs as the delay stage is set up in reflection. The reproducibility of the mechanical stage is absolute and approximately $2 \mu\text{m}$ also. Both the accuracy and reproducibility are of no limitation on our time scale as the pump pulse is longer in time than the errors of the mechanical stage.

In addition, the chopper is also placed in the pump pulse beam path with a 500 Hz blocking repetition rate. Therefore it blocks out every second pump pulse so that the ratio between the pumped and unpumped spectra can be measured. The pump and probe pulses are aligned and overlapped onto the dye layer of the DSSC sample as the indoline dye is photoexcited and probed. The pulses are overlapped in space with the use of a computer optimisation program, and they are overlapped in time by ensuring that their paths are of equal length. The sample is rotated through the pump and probe pulses so not to damage it by re-exciting molecules which have not yet relaxed back to the ground state.

After the sample, the pump beam is directed into a beam dump as the pump pulse is only necessary for photoexcitation. Its spectrum can also be used to assign the pump and probe spectra before they are divided by one another. In addition, by reflecting the beam into a camera, its position can be determined and the vertical and horizontal drift in the laser beam over the experimental time corrected. As shown in figure 4.7, the probe beam is dispersed

in a spectrometer after interacting with the DSSC sample, and the transmitted spectrum of each shot is detected with the use of a line scan camera. The detection process is slow, so the overall temporal resolution is given by the pulse duration and delay accuracy and not by the detector. As can be seen from the setup, the reference probe pulse spectrum is not determined without the sample but only a ratio between the pumped and unpumped spectra is measured. Therefore with the use of this method, no classical absorption spectrum is available.

As previously mentioned, the probe pulse can either be a white light continuum or generated with the use of a second NOPA. A second NOPA was therefore built to provide the ultrafast probe pulse in NOPA - NOPA experiments.

The Non-linear Optical Parametric Amplifier - NOPA

The functionality of the NOPA is shown in figure 4.8 [36]. The incoming pulse is split into two using a 90:10 beam splitter. 10% of the initial pulse is used to generate a white light continuum in a sapphire crystal through non-linear processes in the crystal (WLG). This is the same process as the probe pulse white light generation. The white light pulse is then directed into a β -Barium Borate crystal (BBO 1) to be used as the seed light for the optical parametric amplification. The remaining 90% of the initial pulse is directed through BBO 2 specifically cut at an angle to the plane of incidence to ensure efficient second harmonic generation (SHG) of the incoming pulse of wavelength 775 nm. The generated UV pulse at a centre wavelength of 387.5 nm is directed through an adjustable delay stage before it is aligned to overlap in space and time with the white light pulse in BBO 1.

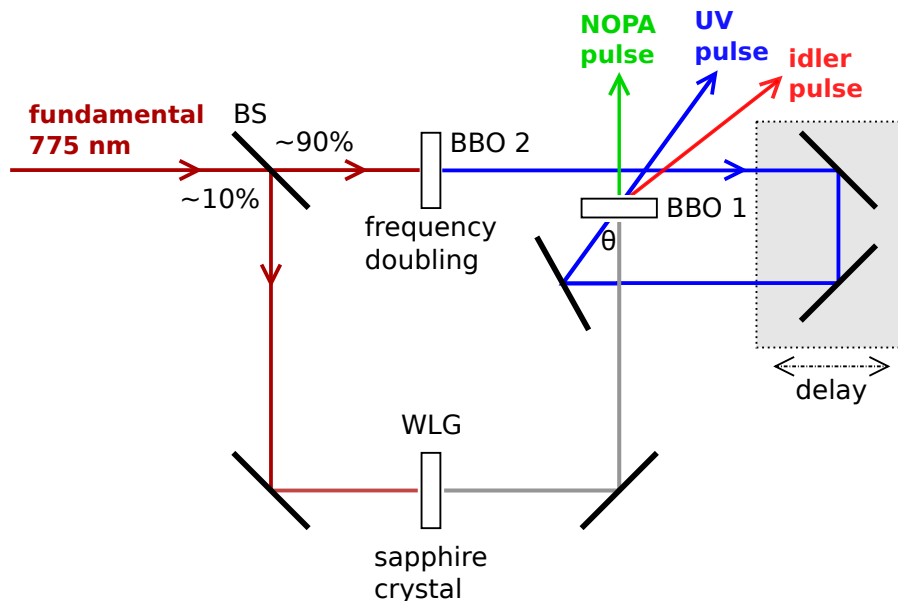


Figure 4.8: The experimental setup of a one amplification stage NOPA showing the crystals used for the non-linear processes as well as the phase matching angle in the horizontal plane. In the actual setup it is aligned in the vertical plane.

The non-linear processes that occur within BBO 1 can be described using the oscillation of electrons in an optically non-linear medium due to an external electric field. The high intensity UV pump pulse causes the electrons along its propagation in the BBO crystal to oscillate with its frequency (ω_P). The weak white light pulse is aligned to overlap with the UV pulse in the crystal thereby also causing the electrons to oscillate with its frequencies.

The phases and polarisation of the white light are perfectly determined by the generating laser pulse. Therefore the oscillation of the electrons with ω_P becomes slightly modulated with the frequencies of the white light. This causes the generation of side bands at the sum and difference frequencies. In the energy/photon picture these are referred to as seeded sum frequency mixing (SFM) and difference frequency mixing (DFM) processes. SFM can be described as $h\nu_P + h\nu_S = h\nu_{SF}$ and DFM as $h\nu_P = h\nu_S + h\nu_I$ where the photon energies correspond to the UV pump pulse (P), the white light seed pulse (S), the sum frequency generated photon (SF) and the difference frequency generated photon which is the idler pulse (I).

The DFM process is referred to as optical parametric amplification and occurs under the condition of phase matching. A frequency pair is chosen by aligning the phase matching angle (θ) in BBO 1 along with using the fact that the white light pulse has a chirp in time (see below) and selecting which wavelengths are amplified. For constructive interference to occur, the velocities of the three waves in the direction of propagation must be equal. Therefore, the phase matching condition for optical parametric amplification can be written as $\vec{k}_P = \vec{k}_S + \vec{k}_I$. The wavelength dependence of the angle between \vec{k}_P and \vec{k}_S can be seen in figure 4.9 [37].

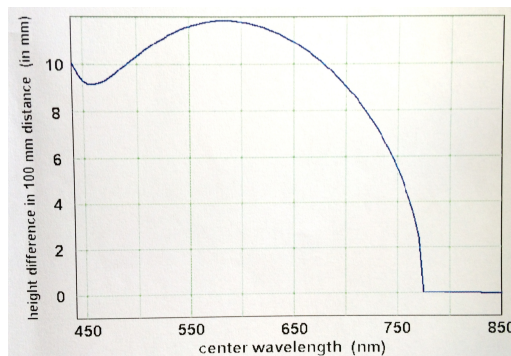


Figure 4.9: A graph depicting the wavelength dependence of the vertical separation between the incoming white light pulse and the UV pulse into BBO 1. From this graph the phase matching angle (θ) can be calculated for a given NOPA pulse central wavelength.

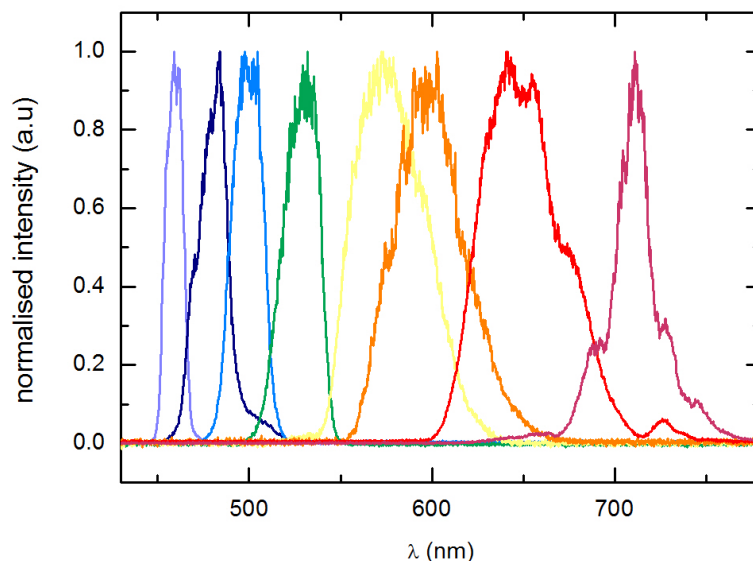


Figure 4.10: Intensity normalised NOPA pulse spectra measured for varying central wavelengths obtained with the use of a two stage NOPA. The pulse durations vary from approximately 50 fs at a central wavelength of 460 nm to sub 30 fs at a central wavelength of 580 nm.

The processes described above form part of a one amplification stage NOPA. The pulse

energy produced with the use of one amplification stage ($10 \mu\text{J}$) is high enough to be used as the probe pulse, but for a pump pulse a two amplification stage NOPA is needed. In the second stage, the first stage pulse is used as a seed pulse instead of the white light therefore causing further amplification and generating higher energy pulses ($20\text{-}30 \mu\text{J}$).

With the use of this NOPA, broadband pulses with a central wavelength between 470 nm and 700 nm and a spectral width of 5-7% can be generated, see figure 4.10. Since the spectral bandwidth of the seeding white light continuum portion can be large, and phase matching can be achieved within this bandwidth, the generated pulses can be compressed to significantly shorter than the fundamental laser pulse (150 fs).

Compressing a Pulse

The lengthened NOPA pulses are compressed with the use of a two-prism compressor as shown in figure 4.11. The prisms are rotated to the Brewster angle of the central wavelength (θ_B) to ensure maximum transmittance and little to no reflection. After exiting the NOPA, the pulses have a positive linear chirp in time corresponding to normal dispersion. The two-prism compressor creates a negative linear chirp (anormal dispersion) to compress the pulse.

As the beam is directed through prism 1, the longer wavelength components of the pulse travel faster than the shorter wavelength components as the index of refraction of the prisms is wavelength dependent. This causes the shorter wavelengths to bend more than the longer wavelengths upon exiting prism 1 and the pulse to spread out spatially before being collimated by prism 2 as shown in figure 4.11. The bases of the two prisms must be parallel for collimation to be achieved. A mirror is used to direct the pulse back along the same path. The short wavelength (bluer) components travel longer distances in both air paths, while the long wavelength (redder) components travel a longer distance, but at the same time faster in prism 2. By changing the distance between the two prisms and the position of prism 2 an overall negative chirp can be created and the pulse compressed to sub 50 fs.

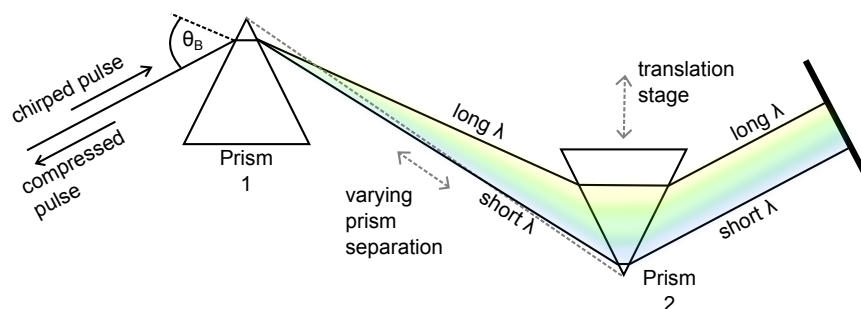


Figure 4.11: A two-prism compressor is used to compress a chirped green NOPA pulse to sub 50 fs. The prism separation is varied depending on the central wavelength of the incoming pulse. The translation stage of prism 2 is used to alter the relative path length of the different wavelength components within the pulse.

The incoming and outgoing beams are separated vertically with the use of the mirror in figure 4.11. Before the compressed outgoing pulse is directed to the sample via the mechanical delay stage and chopper, its duration is measured using an autocorrelator.

Taking an Autocorrelation

The setup of the autocorrelator used to measure the pulse duration is depicted in figure 4.12. The incoming pulse is split into two identical parallel pulses with the use of two D-mirrors, one of which is mounted on a mechanical translation stage. One of the benefits of our autocorrelator setup is that no beam dispersion occurs from a beam splitter. However, the use of the D-mirrors to split the incoming pulse into two also has the disadvantage that it depends on a neat input beam mode, otherwise pulses 1 and 2 are unevenly weighted. The two pulses are then focused in a BBO crystal with the use of an off-axis parabolic mirror ensuring that no spherical aberration takes place.

If the crystal is orientated at the phase matching angle for the incoming pulse's wavelength, frequency doubling can occur proportional to the intensity of the incoming pulse. Therefore the BBO crystal is mounted so that it can be rotated easily. In addition, a very thin crystal is used (3mm) such that it has a broad phase matching acceptance. This is necessary for the autocorrelation of ultrashort broadband pulses. In our situation, the frequency doubling process converts two visible photons of equal frequency (ω) into one UV photon of double frequency (2ω). If the two photons originate from pulse 1, the UV photon will be created in the beam path of pulse 1. Similarly the UV photons created from pulse 2 will be found in the beam path of pulse 2. A third scenario involves an ω photon from pulse 1 and an ω photon from pulse 2 forming a 2ω photon. In this case, to conserve momentum, the resulting frequency doubled photon is emitted in the bisecting direction (autocorrelation pulse).

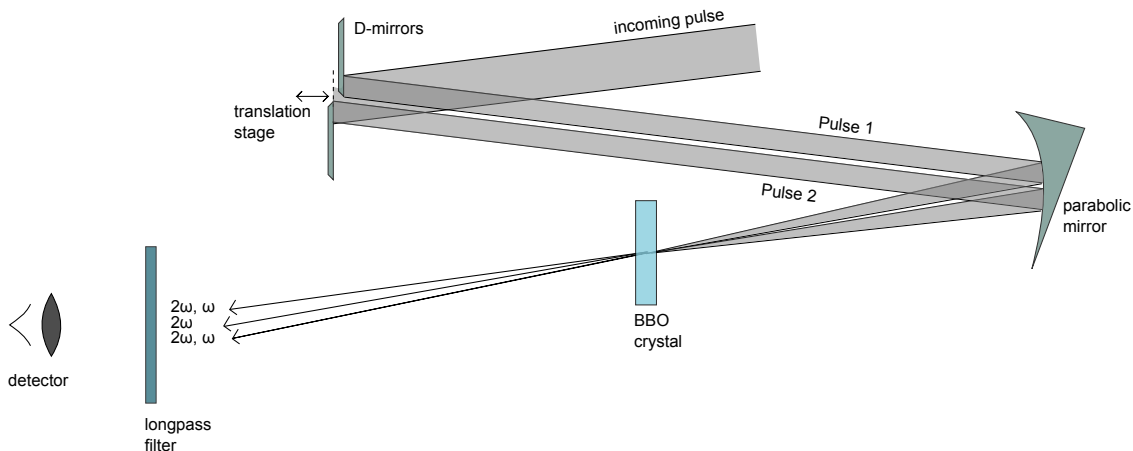


Figure 4.12: The setup of an autocorrelator used to measure pulse duration. The D-mirrors and focusing mirror are used as they are broadband and allow ultrashort pulse duration measurements.

As long as the autocorrelation pulse exists, pulses 1 and 2 overlap both temporally and spatially in the crystal. The delay between the pulses is then varied with the use of the mechanical translation stage and the intensity of the autocorrelation pulse is measured using a photomultiplier tube as a function of the delay stage distance. In this way the temporal overlap between pulse 1 and 2 is determined as a convolution. The pulses are assumed to be Gaussian-like, and as can be seen in figure 4.13 the convolution of two Gaussian pulses is also a Gaussian pulse. From the convolution the full width at half maximum (FWHM_C) can be determined and with the use of equation 4.2.3, the pulse duration (FWHM_P) is calculated for the initial pulse as

$$\text{FWHM}_P = \frac{\text{FWHM}_C}{\sqrt{2}}. \quad (4.2.2)$$

The deconvolution factor ($\frac{1}{\sqrt{2}}$) for two identical Gaussian pulses is determined from the intensity autocorrelation function

$$S(\tau) = \int_{-\infty}^{\infty} I_1(t)I_2(t - \tau)dt \quad (4.2.3)$$

where $S(\tau)$ is the measured autocorrelation intensity as a function of pulse separation τ . $I_1(t)$ is the intensity distribution of pulse 1 and $I_2(t - \tau)$ the intensity distribution of pulse 2 which is shifted by τ with the use of the translation stage.

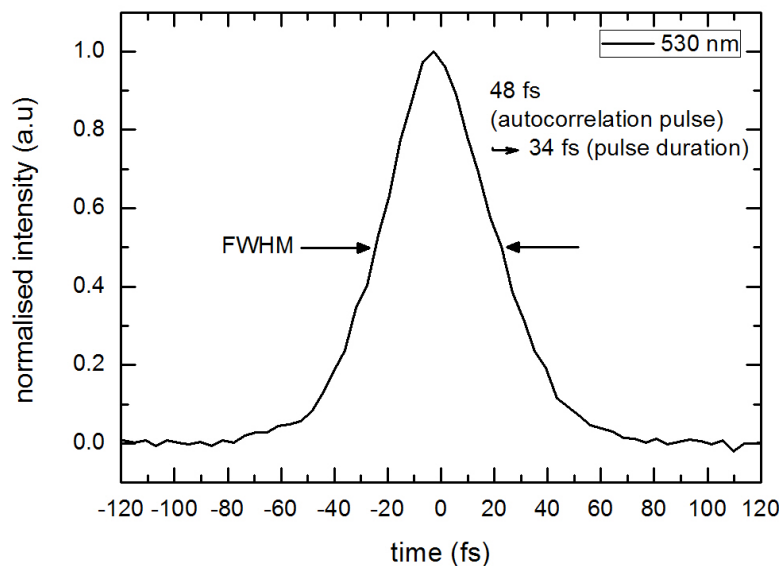


Figure 4.13: A typical autocorrelation spectrum of a NOPA pulse with central wavelength of 530 nm and bandwidth of approximately 15 nm. With the use of this spectrum the FWHM can be determined for a pulse.

With the use of an autocorrelator, the NOPA pulse duration can be determined and reduced to sub 50 fs before it is used as the pump or probe pulse in an experiment. The white light continuum is longer in time and therefore limits the resolution of the measurement.

White Light Generation

A white light continuum can be generated in a sapphire crystal through a non-linear process with the use of high intensity ultrashort laser pulses [38]. In a non-linear optical process, the polarisation depends on the electric field of the incoming light wave in a non-linear manner. Therefore when the electric field of the incoming light wave has a similar magnitude as the sapphire crystal's atomic force, the non-linear parts of the polarisation become important. The non-linear polarisation terms are responsible for new physical characteristics which are observed in the crystal. The polarisation depends on the electric field of the incoming wave according to equation 4.2.4, where $\tilde{P}(t)$ is the polarisation vector, $\tilde{E}(t)$ the incoming electric field and $\chi^{(n)}$ the susceptibility

$$\tilde{P}(t) = \chi^{(1)}\tilde{E}(t) + \chi^{(2)}\tilde{E}(t)^2 + \chi^{(3)}\tilde{E}(t)^3 + \dots \quad (4.2.4)$$

A sapphire crystal is a centrosymmetric medium. Therefore the even order terms are zero in the above expression and the lowest non-linear term in the polarisation expansion is the third order term. This cube term is responsible for self focusing of the incoming laser beam as well as self phase modulation (SPM), the two processes responsible for white light continuum generation [39; 40].

Self focusing can be explained with the use of the equation $n = n_0 + n_2 I(r, t)$ for the refractive index (n) of a medium with Kerr non-linearity. This equation is derived from the polarisation expansion (equation 4.2.4) with n_0 the field-free nonperturbed refractive index of the medium, n_2 the frequency dependent non-linear refractive index, and $I(r, t)$ the spatial and time dependent intensity of the laser pulse [41].

The laser beam has a Gaussian shaped intensity profile. Therefore it is most intense in the centre and the non-linear index of refraction observed in a medium is higher for the middle of the beam. This results in the beam travelling slower in the centre and focusing. To aid with self focusing, the incoming laser beam is focused into the sapphire crystal with the use of a lens. A threshold power determined by the sapphire crystal properties as well as the incoming beam wavelength must also be overcome. If the threshold power is not reached, self focusing does not occur and no continuum generation can take place.

Moreover, self focusing is limited by the wavelength of the laser beam through diffraction therefore defocusing the beam and stopping it from merging to one point. When the self focusing is balanced out by the defocusing, the beam is collimated.

Self focusing causes the laser beam profile to decrease therefore increasing the intensity and enhancing self phase modulation. SPM is created due to the time dependence of the intensity term used to calculate the non-linear index of refraction. For a better understanding refer to appendix B. An increase in the beam intensity with time causes a red shift in the incoming beam, while a decrease in intensity causes a blue shift. The time variation in intensity therefore causes many new wavelengths to be created from an almost monochromatic source.

As a result of this process, the different spectral components of the generated white light continuum become separated in time within the pulse. This chirp increases by normal dispersion on the sapphire crystal and lens material to a significant amount which needs to be corrected. So even though the fundamental laser pulse used for white light generation is 150 fs long, the generated continuum is chirped in time to approximately 1 ps with each spectral component about 150 fs long.

Chirp Correction

The previously mentioned chirp in the white light pulse can be observed in our transient absorption measurements as in figure 4.14. This is corrected manually by shifting the time zero of each wavelength to coincide.

The thickness of the chirp visible in the transient spectrum is determined by the convolution of the pump and probe pulses. At time zero, the pump and probe pulses overlap in the sample both in time and space. Therefore their correlation determines the time resolution of the transient absorption measurement. A NOPA pump - WL probe measurement has a time resolution sub 200 fs as each spectral region making up the 1 ps white light pulse is about 150 fs long even though the NOPA pulse is sub 50 fs. For improved resolution NOPA pulse - NOPA probe measurements are taken, where resolutions of sub 100 fs can be achieved.

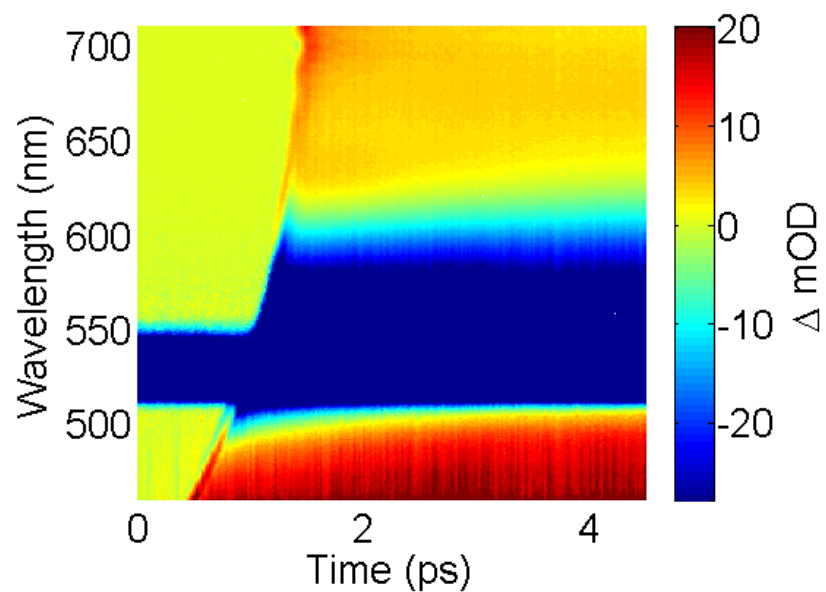


Figure 4.14: The short time window transient absorption spectra measured for a DN91 DSSC sample with 530 nm pump pulse and a white light continuum probe pulse. The white light chirp in time is clearly visible.

5. Transient Absorption Measurements

With the use of the experimental techniques described in chapter 4, ultrafast transient absorption (UTA) spectroscopy measurements were taken on DSSC samples sensitised with one of three previously mentioned indoline dye derivatives, DN285, DN216 and DN91, see figure 5.1.

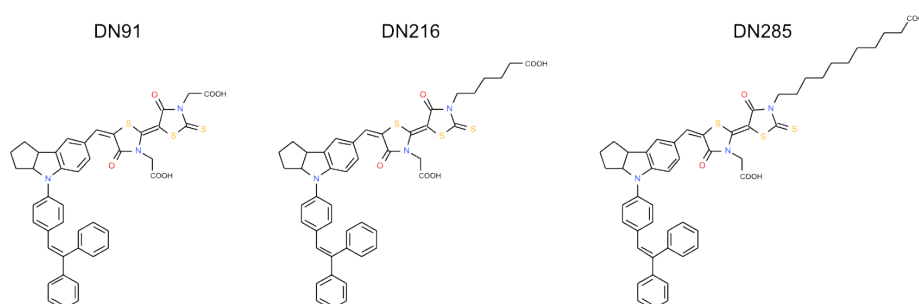


Figure 5.1: Chemical structures of the indoline dyes DN285, DN216 and DN91.

From the transient absorption spectra, decay constants and relative changes in population were obtained and compared for the excited state absorption, ground state bleaching and oxidised dye absorption signals of the three dyes. By relating signal decays to charge transfer processes we were able to assign time constants to the various dynamics which occur within the DSSCs. Measurements were taken on fully operational solar cells under short circuit conditions and with an applied external potential. Before any UTA spectroscopy measurements were taken, the steady state absorption spectra of the three dyes adsorbed to ZnO were measured, see figure 5.2. From the results, the DSSC samples were pumped with a sub 50 fs laser pulse of central wavelength of 530 nm generated with a NOPA (bandwidth approximately 40 nm). This wavelength corresponds to the $S_1 \leftarrow S_0$ absorption maxima of the dyes – approximately 530 nm for all three, marked with vertical lines in the figure. The high absorption edge in the UV is characteristic of the ZnO thin film.

The pump-probe measurements were first carried out with a white light continuum as the probe pulse. In this way, we were able to observe changes in the absorption spectrum of the solar cells with a spectral range from 450 nm to 720 nm. As previously mentioned, the somewhat limited NOPA pump - WL probe temporal resolution (sub 200 fs) is determined by the convolution between the pump pulse and each spectral component of the white light pulse. To achieve a higher temporal resolution (sub 100 fs), measurements were also taken with a second NOPA as the probe pulse. In this way a smaller spectral region of approximately 100 nm around the probe pulse central wavelength was observed.

5.1 Transient Absorption Spectra

Long time window (300 ps) transient absorption spectra were taken in 1 ps increments for the three solar cell samples, each sensitised with one of the indoline dyes, see figure 5.3. As previously explained, the blue ground state bleaching (GSB) signal is observed at approximately 550 nm (in the wing of the pump pulse) and the red overlapping excited state absorption of the neutral dye (ESA) and absorption of the oxidised dye (OX) signals at central wavelengths of 675 nm and 480 nm. The full ESA signal is not observed on this time scale as its initial

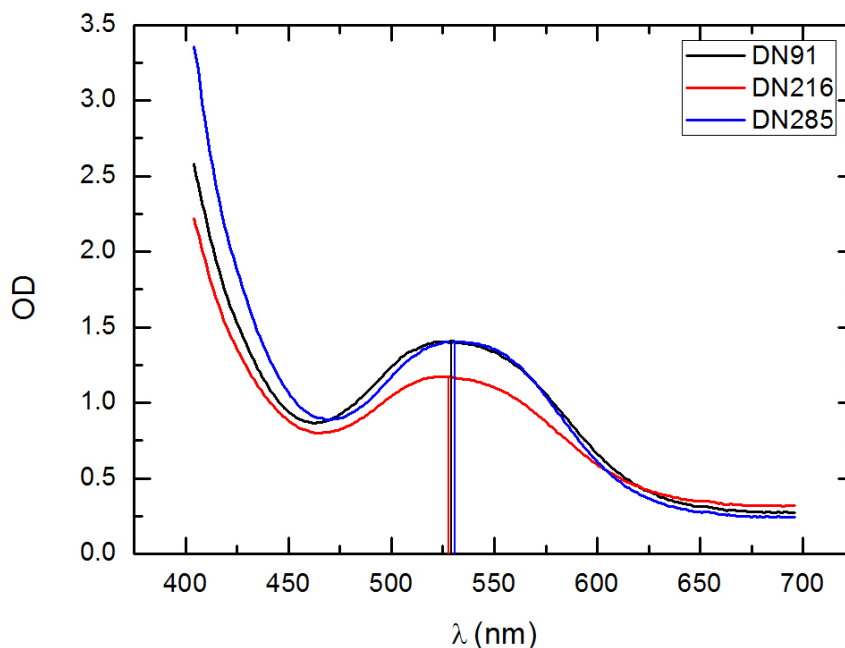


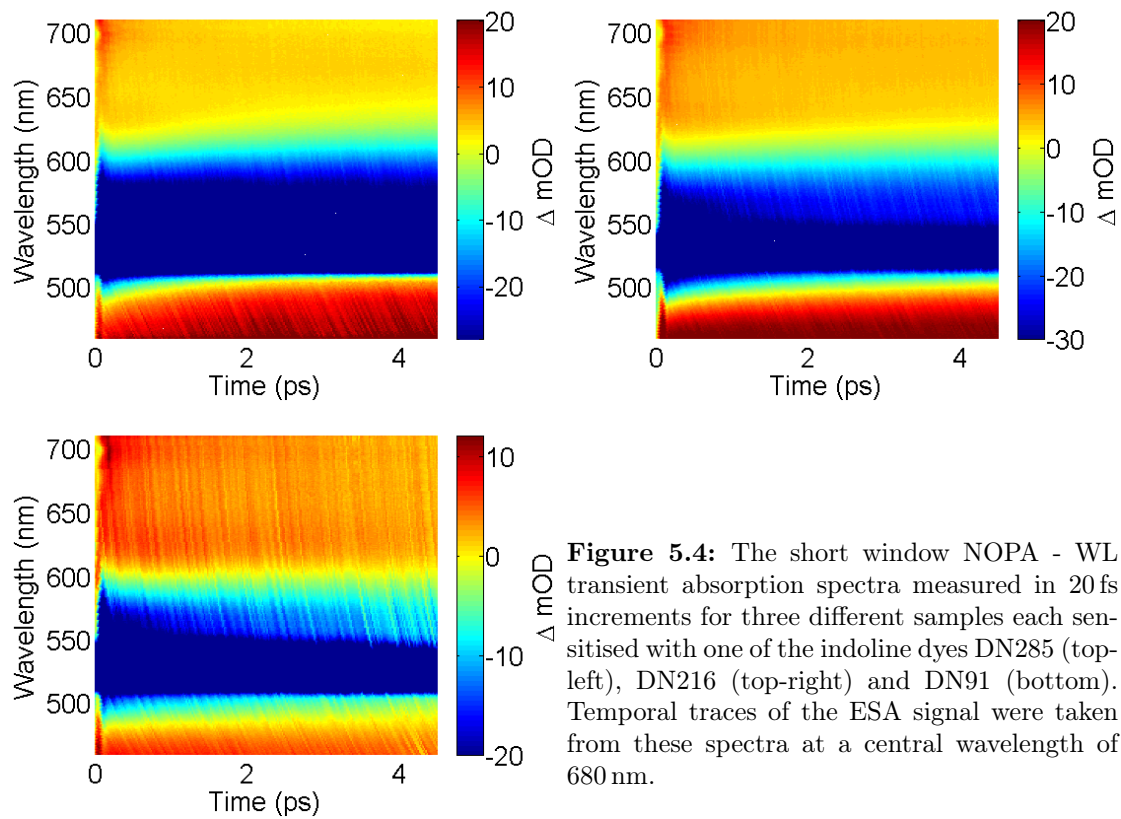
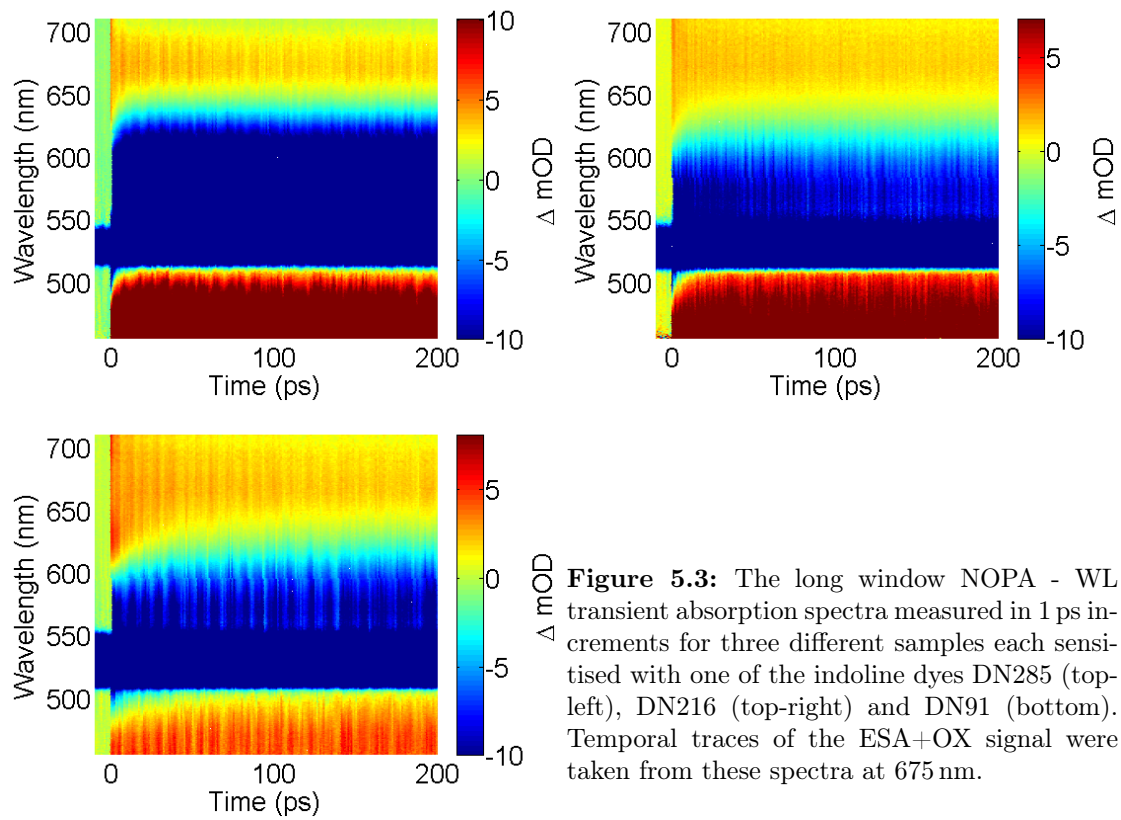
Figure 5.2: Steady state spectra of the indoline dyes DN91, DN216 and DN285 sensitised to ZnO. All the dyes exhibit their $S_1 \leftarrow S_0$ broad absorption maxima around $\lambda = 530$ nm. The strong absorption in the UV is characteristic of ZnO.

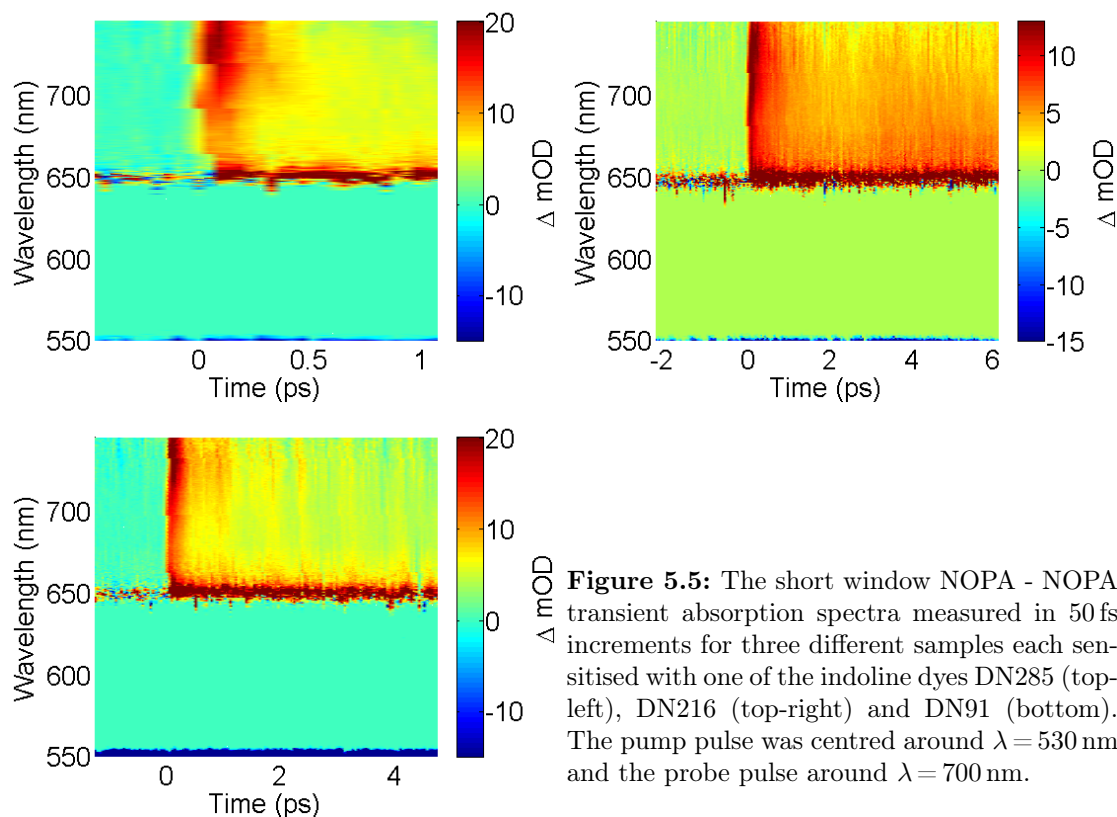
decay, corresponding to the injection time from the dye into the ZnO, occurs two orders of magnitude faster.

By comparison of the transient absorption spectra, the charge dynamics in the three samples look similar. Each of the indoline dyes exhibits GSB, ESA and OX signals. In addition, a spectral shift of the ESA+OX signal to a higher central wavelength is visible in the spectra. It appears that this shift occurs on a faster time scale for DN91 than for DN216 than for DN285, as will be investigated later on. To be able to resolve ultrafast electron kinetics within the solar cells, such as the fast ESA decay and therefore determine a dye to ZnO injection time, additional measurements are required and were taken with a short time window (5 ps) in 20 fs increments, see figure 5.4.

From comparison of the three absorption spectra of figure 5.4, we can see that all three samples, each sensitised with a different dye, show an ultrafast ESA signal at approximately 675-680 nm. The spectral shift is not visible in these measurements as the time window is too short.

To better temporally resolve the ultrafast decay (sub 100 fs), NOPA pump - NOPA probe measurements were also taken in 50 fs increments, see figure 5.5. For these short time window scans the pump NOPA pulse was generated at a central wavelength of 530 nm and the probe NOPA pulse at a central wavelength of 700 nm, as the ultrafast dynamics are observable around this wavelength. This is the furthest to the near infra-red that we can tune the NOPA. In this case, the resulting transient spectra provided no additional information to the UTA spectra taken with the white light continuum probe pulse. Therefore the NOPA - WL spectra were used for further investigation as they cover a wider spectral region. To be able to determine the decay time constants and amplitudes of the signals in the transient absorption spectra shown here, we took horizontal lineouts (plotted as ΔOD versus time) at the central wavelength of the signal of interest.





5.2 Horizontal Lineouts

To learn more about the injection efficiencies of the three indoline dyes into ZnO, we compare the decay constants as well as the relative amplitudes of the ESA+OX and GSB signals. Horizontal lineouts were taken from the transient absorption spectra at 680 nm and 675 nm for the ESA+OX short and long time window measurements respectively, and 570 nm for the GSB signal. All the traces were fitted with exponential decay functions, see figures 5.6, 5.7 and 5.8.

Short Time Window Scans

The short time window traces plotted in figure 5.6 were fitted with a bi-exponential fit

$$f(t) = A_0 + A_1 \exp\left(-\frac{t}{\tau_1}\right) + A_2 \exp\left(-\frac{t}{\tau_2}\right), \quad (5.2.1)$$

where A_0 is the baseline amplitude, and the two decay time constants τ_1 and τ_2 with their respective amplitudes A_1 and A_2 . Each trace was obtained from the transient spectra of the three DSSCs sensitised with one of the indoline dyes DN91 (black), DN216 (red) and DN285 (blue). τ_1 is the time constant of the ultrafast ESA decay corresponding to the femtosecond injection time of the photoexcited electrons into the ZnO conduction band. As electrons are injected from the LUMO of the dye into the conduction band of the ZnO, the ESA signal decays. τ_2 occurs on a picosecond time scale and corresponds to a slower electron injection by the excited dye into what is believed to be ZnO surface trap states, also causing the ESA signal to decay. The femtosecond injection times (τ_1) for the three dyes are different from one another. The DN91 dye has the fastest injection time into the ZnO conduction band of $175 \text{ fs} \pm 9 \text{ fs}$. A longer injection time was obtained for DN216 of $194 \text{ fs} \pm 20 \text{ fs}$. Lastly, the longest injection time of $259 \text{ fs} \pm 27 \text{ fs}$ was determined for DN285. Therefore, apparently, the

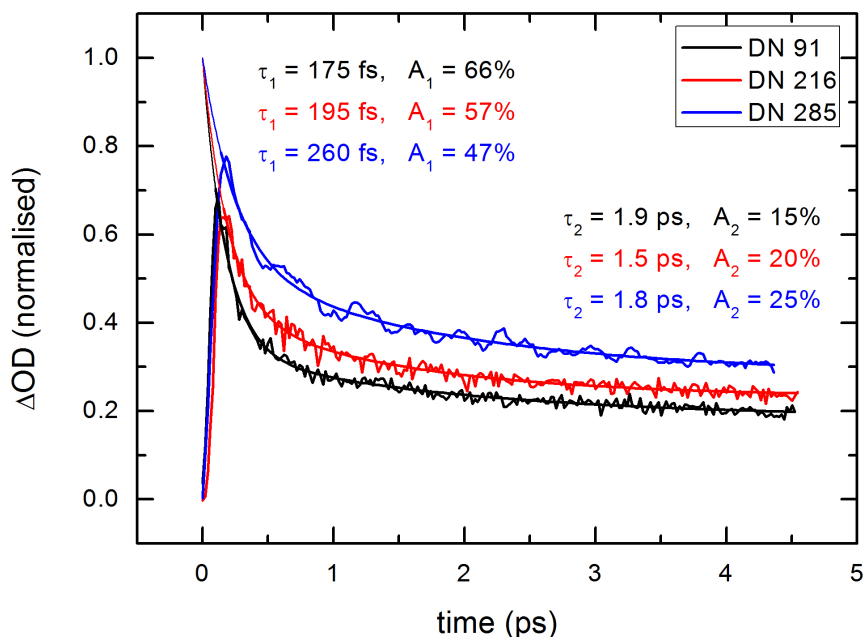


Figure 5.6: Short time window temporal traces of ESA fitted with bi-exponential fits taken at 680 nm from the transient spectra of figure 5.4. The data and fits were normalised to the $t = 0$ value of the fits respectively for DN285 (blue), DN216 (red) and DN91 (black).

excited dye to ZnO conduction band injection time (τ_1) increases with increasing alkyl chain length.

In the same way, the picosecond injection times (τ_2) into the ZnO surface trap states can also be compared for the three dyes. They are $1.9 \text{ ps} \pm 0.3 \text{ ps}$, $1.5 \text{ ps} \pm 0.2 \text{ ps}$ and $1.8 \text{ ps} \pm 0.3 \text{ ps}$ for DN91, DN216 and DN285 respectively. By taking the errors into consideration the three decay constants do not differ from one another. This suggests that the injection time into the ZnO surface trap states is independent of the alkyl chain length of the three indoline dyes investigated.

As can be seen in figure 5.6, the decays were fitted from their maximum ΔOD data points and the fits extrapolated to time t_0 . Both the experimental data as well as the fits were normalised to the t_0 ΔOD value (maximum value) of each of the fits. The extrapolation of the fit functions to t_0 was necessary to overcome the time resolution limitations of our experiment. At time t_0 , the pump and probe pulses are simultaneously interacting with the sample – their convolution determining the time resolution. Although the rise time of the ESA signals (corresponding to the photoexcitation time of the indoline dye) is ultrafast, and the injection of electrons to the ZnO begins instantaneously, the time resolution of our measurement causes the ESA absorption decays to only be measured after approximately 150 fs. By this time in the measurement, the amplitudes of the ultrafast injection to the ZnO have already decayed by a significant percentage. Therefore, the relative amplitudes of the two injection times for each of the three dyes, were determined after plotting the fits to time t_0 . The relative changes in population of molecular states (amplitudes) can then be used together with the injection time constants to determine the injection efficiencies of the three dyes in the context of fully operational DSSCs.

The amplitudes of the two injection pathways for the three indoline dyes are determined together with the baselines of the fits in order to learn something about the relative number of

electrons injected through the two possible path ways. The amplitudes denoted A_1 correspond to the ultrafast injection (τ_1) into the conduction band of the ZnO. When compared, we see that the amplitude of the DN91 femtosecond injection is the highest (66%) followed by DN216 (57%) and DN285 (47%). The trend that a higher amplitude corresponds with a faster injection time suggests that the femtosecond injection was most efficient for the dye with the shortest alkyl chain length (DN91) and least efficient for the dye with the longest alkyl chain length (DN285), both into the conduction band and surface trap states of ZnO.

The amplitudes, A_2 , correspond to the picosecond injection time that is thought to take place via the surface trap states of ZnO. When compared, the lowest amplitude is associated with the DN91 picosecond injection (15%) followed by DN216 (20%) and DN285 (25%). As the picosecond injection time constants τ_2 were, within error, the same for all three dyes, the difference in amplitudes is rather a result of the efficiency of the ultrafast injection. Therefore the dye with the most efficient femtosecond injection, DN91 (shortest alkyl chain), has the lowest picosecond injection amplitude A_2 as there are fewer photoexcited electrons left after the ultrafast injection. On the other hand, DN285 (longest alkyl chain) has both the least efficient femtosecond injection as well as the highest picosecond injection amplitude A_2 resulting from more photoexcited electrons left after the ultrafast injection. The average length alkyl chain dye, DN216, completes the trend.

In addition, the baseline amplitudes (A_0) of the three decays fitted can also be used as an indicator of overall injection efficiencies of the three indoline dyes. DN91 (shortest alkyl chain) has the lowest baseline amplitude (19%) followed by DN216 (23%) and DN285 (longest alkyl chain length) with the highest baseline amplitude (28%). These values indicate that after the injection has taken place, following both paths, the excited state absorption signal is strongest for DN285 (most electrons left over in LUMO) and weakest for DN91 (least electrons left over in LUMO). Therefore the overall injection decreases in efficiency as the alkyl chain of the second carboxyl anchor group increases in length.

Long Time Window Scans

The long time window traces for the three dyes, plotted in figure 5.7, were extracted as horizontal lineouts at a central wavelength of 675 nm from the transient absorption spectra of figure 5.3. The traces were fitted with bi-exponential fits and the decay constants and relative amplitudes determined. Both the decays and fits were normalised to the baseline amplitudes obtained in the short time window scans ($A_3 + A_4 = A_0$). This was done as the 1 ps increments of the long time window scans are too large to detect femtosecond scale decays. Additionally the first few data points (3-4 ps) were omitted from the fits and data. With the use of the fit functions, relative amplitudes were calculated for the picosecond dynamics in relation to the maximum value of the femtosecond fits – therefore in terms of the full ESA and OX signals.

The two decays observed in the long time window scans can be attributed to two separate signals which unfortunately appear at the same central wavelength – the excited state absorption of the neutral dye molecules together with the absorption of the oxidised dye molecules. The faster time constant τ_3 corresponds to the radiationless decay of the ESA signal as photoexcited electrons relax back to the ground state of the dye. This decay is mirrored in the ground state bleaching signal as the ground state becomes more populated, see below. The τ_3 time constants (relaxation times) and corresponding amplitudes A_3 differ from one another in the following way. The dye DN91 has the slowest relaxation time of $39 \text{ ps} \pm 4 \text{ ps}$ and the smallest overall relative amplitude of 5%. DN216 has a faster relaxation time of $30 \text{ ps} \pm 5 \text{ ps}$ with a larger relative amplitude of 6%. Following the trend, DN285 has the fastest relaxation time of $26 \text{ ps} \pm 2 \text{ ps}$ together with the largest relative amplitude of all three dyes of 13%. While the time constant τ_3 displays a faster relaxation time with increasing alkyl chain length, its

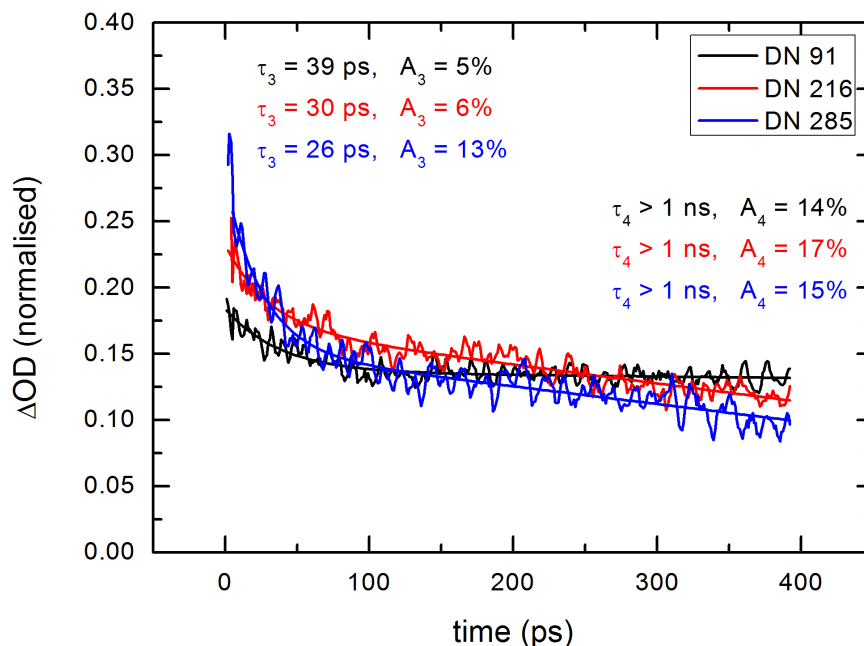


Figure 5.7: Long time window temporal traces of ESA+OX fitted with bi-exponential fits taken at 675 nm from the transient spectra of figure 5.3, DN285 (blue), DN216 (red) and DN91 (black). The fits and data were normalised to the baseline amplitude (A_0) of the short time window temporal traces and the first 4 ps of the dynamics were omitted.

corresponding amplitude A_3 exhibits a trend of higher amplitude as the alkyl chain length increases.

Generally a faster kinetic process is preferred by electrons, so a faster signal decay time should naturally correspond to a higher amplitude, as was observed with the ultrafast injections (τ_1 , A_1) into the ZnO conduction band. However, as τ_3 is the slowest of three ESA decays, we must take into account the injection times (τ_1 and τ_2) and amplitudes (A_1 , A_2 and A_0) when trying to explain the trend in relaxation amplitudes A_3 for the three dyes.

By looking at the baseline amplitudes ($A_0 = A_3 + A_4$) of the femtosecond scans (normalisation values for picosecond scans), we see that the baseline amplitude for DN285 is the highest and DN91 is the lowest. This indicates that DN285 had the most photoexcited electrons in the LUMO left after injection. Therefore more electrons could relax back to the ground state causing a high A_3 amplitude. On the other hand, DN91 had the least amount of electrons left in the excited state after injection. Therefore the least amount of photoexcited electrons were available to relax back to the ground state, resulting in the smallest A_3 amplitude.

The longest time constant τ_4 corresponds to the decay of the oxidised dye absorption signal (OX) due to regeneration from the redox couple in the electrolyte solution. For all three dyes this time constant is in the order of nanoseconds and therefore too long to be measured accurately with our experimental method.

Both this OX signal decay as well as the ESA relaxation are mirrored in the GSB signal, see figure 5.8. Time constants of $47 \text{ ps} \pm 7 \text{ ps}$ (DN91), $29 \text{ ps} \pm 6 \text{ ps}$ (DN216) and $22 \text{ ps} \pm 4 \text{ ps}$ (DN285) were obtained for τ_3 , in addition to nanosecond scale time constants corresponding to τ_4 . The GSB horizontal lineouts were taken at a central wavelength of 570 nm, in the wing of the ground state bleaching signal. The traces could not be taken at the central wavelength of the GSB signal as it is covered by the pump beam scattered light.

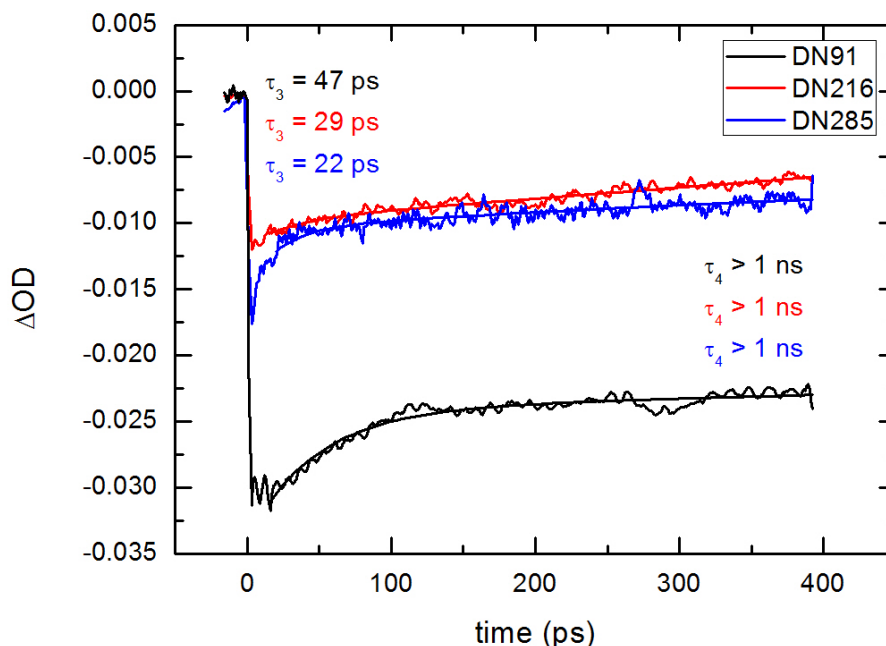


Figure 5.8: Long time window temporal traces of GSB fitted with bi-exponential fits taken at 570 nm from the transient spectra of figure 5.3, DN285 (blue), DN216 (red) and DN91 (black). The fits and data were not normalised.

The traces in figure 5.8 were not normalised as their amplitudes are our only quantitative indicator of the number of excited molecules in the sample. As can be seen 3%, 2% and 1% of the area probed by the white light continuum was excited for DN91, DN216 and DN285 respectively. As we do not know the fluence precisely, we are not able to compare the cross-sections (x_s) for the three dyes. The absorbance values are highly dependent on the laser pump pulse energy (set to 60 nJ) as well as on the spatial overlap of the pump and probe pulses in the sample and therefore all we can deduce is that more DN91 molecules were excited.

As we normalised the long time window traces to the baselines of the short time window traces, we are able to 'stitch' together a full ESA+OX signal, see figure 5.9 for an example from the DN91 sensitised solar cells' measurements. The normalised ΔOD values on the y-axis were plotted on a logarithmic scale to better visualise the four, vastly different, time constants in one plot. In this way, it is easy to see that if the relaxation amplitude A_3 is small, the amplitudes $A_1 + A_2$ and A_4 will be large, and vice versa. Oxidised dye molecules are created in the sample by the injection of electrons from the photoexcited dye to the ZnO. Therefore the ratio $\frac{A_1 + A_2}{A_4}$ is approximately constant for all three dyes

$$\frac{81\%}{14\%} = 5.8 \approx \frac{77\%}{17\%} = 4.5 \approx \frac{72\%}{15\%} = 4.8. \quad (5.2.2)$$

Moreover, the most efficient injection (largest $A_1 + A_2$) should yield the most oxidised dye molecules (largest A_4) and the lowest relaxation amplitude A_3 . This is indeed the case as can be seen for DN91 in comparison to DN216 and DN285.

The dependence of the trend in injection efficiency on the alkyl chain length of the three indoline dyes directly correlates with the trend observed in the I-V curve measurements on the three variations of DSSCs. It can be used as one explanation towards the variation in short circuit currents as the dye with the shortest alkyl chain and most efficient electron

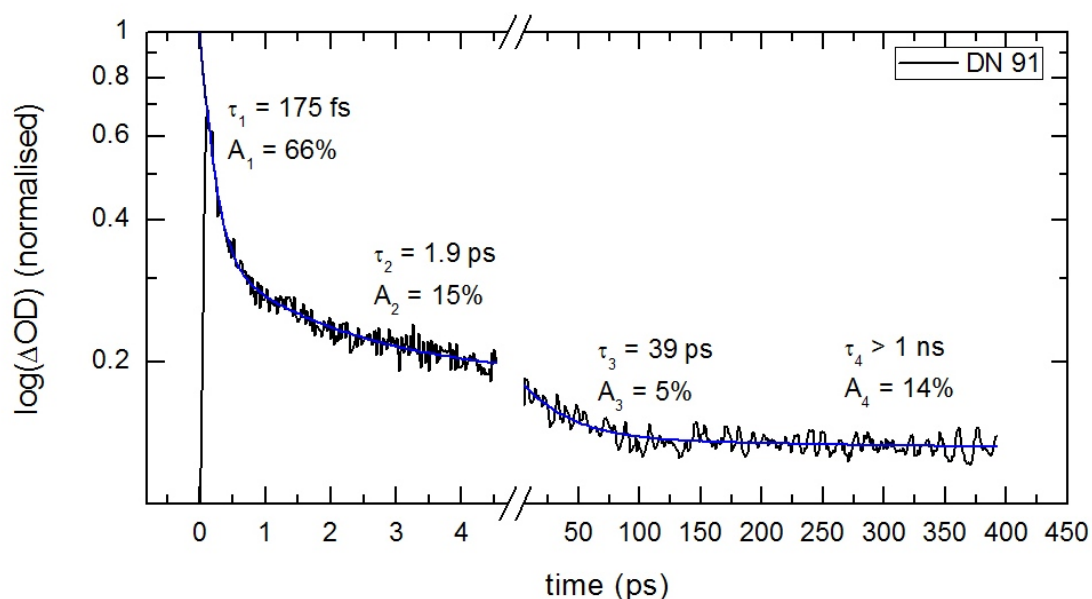


Figure 5.9: A full temporal trace (long and short time window) of the ESA+OX signal corresponding to a DN91 sensitised solar cell as an example. The ΔOD values on the y-axis are plotted on a logarithmic scale for better inclusion of the four decay processes extracted from this signal.

injection (DN91) also produces the highest J_{SC} , see figure 5.10. As the alkyl chain length is increased (DN216 followed by DN285) the injection efficiency drops and so does the short circuit current.

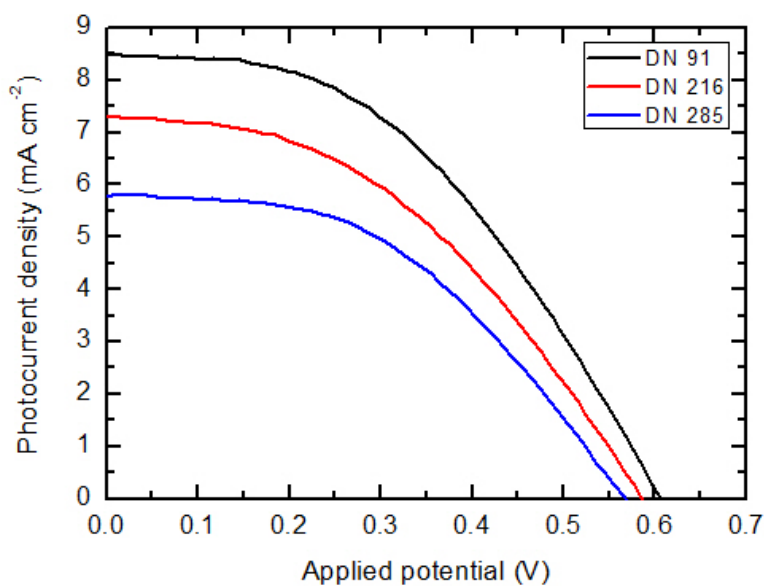


Figure 5.10: Three example light I-V curves of samples made in the same way each sensitised with one of three indoline dyes, DN91 (black), DN216 (red), DN285 (blue).

5.3 UTA Measurements on D149 Sensitised Solar Cells

For the purpose of completeness, and to determine how the double carboxyl anchor indoline dyes compare to the one anchor dye, D149, we re-analysed the UTA spectroscopic data measured previously for a D149 sensitised solar cell [42]. The D149 cells investigated were produced using the same method described in the previous chapters, however the I^-/I_3^- redox electrolyte solution was replaced by inert N_2 gas. In this environment, the electron injection and intramolecular relaxation processes are still observable. In this case, the regeneration of oxidised dye molecules no longer occurs from the redox couple, but from recombination from ZnO, a process with time scale greater than 1 ns. Horizontal lineouts were taken from the D149 short and long time window transient absorption spectra at 680 nm and 675 nm respectively. They were both fitted with bi-exponential fits and plotted alongside the temporal transients of the double anchor dyes, see figure 5.11.

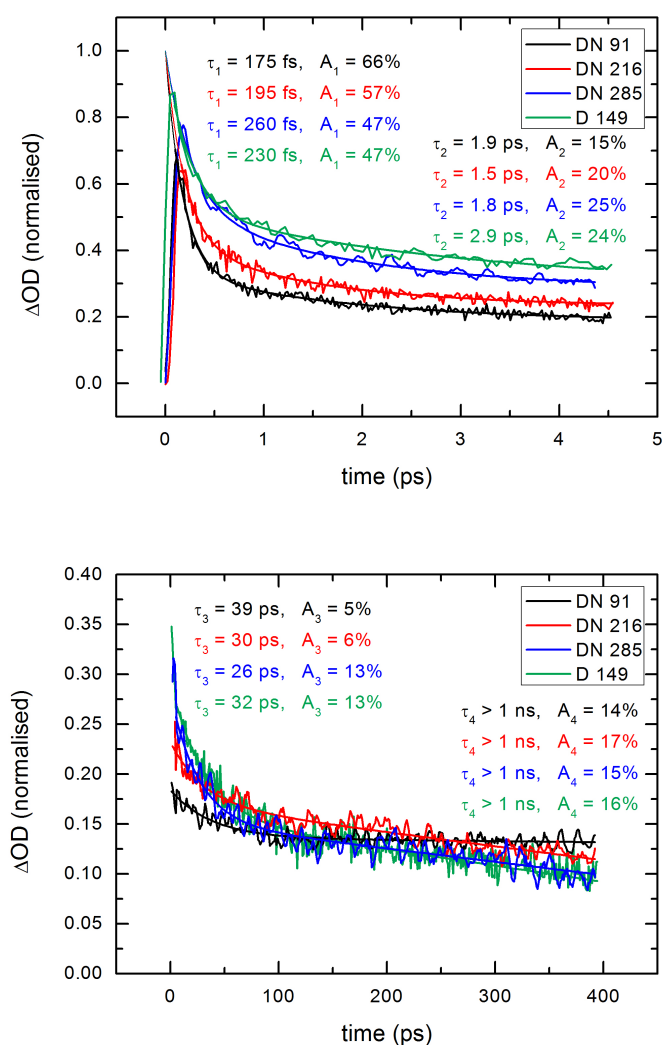


Figure 5.11: Temporal transients taken at 680 nm for the short time window scans (top) and 675 nm for the long time window scans (bottom) from the transient spectra of the solar cells sensitised with DN91 (black), DN216 (red), DN285 (blue) and D149 (green). All the decays were fitted with bi-exponential fits.

From figure 5.11, we can see that the indoline dye D149 (only one carboxyl anchor) behaves very similar to the dye molecule DN285 when sensitised to ZnO as part of a DSSC. All four decay time constants and corresponding amplitudes are approximately the same as DN285. This indicates that the addition of a second carboxyl anchor group greatly improves the stability of the indoline dye adsorbed to the ZnO thin film, without compromising the injection efficiency. In contrast, injection efficiencies were improved for indoline dyes with two anchor groups bonded to short alkyl chains, as in the case of DN91 and DN216. This may indicate that the injection mechanism changes with the addition of the second carboxyl anchor group. For DN91 (shortest alkyl chain) and DN216 (medium alkyl chain) the ultrafast injection could occur with the aid of the -COOH group. The second anchor could bring the chromophore closer to the ZnO therefore reducing the average tunnelling and increasing the injection efficiency [26]. It however no longer has an effect for DN285 (longest alkyl chain) as the second anchor could simply be too far away to assist in the injection and D149 (no second anchor) as it has no second anchor.

5.4 Spectral Shift

In addition to the charge transfer information which can be extracted from fitting horizontal lineouts of the three ESA+OX signals, a spectral shift can also be observed in the long time window transient absorption spectra, figure 5.3. From the spectra we can see that the ESA+OX signal shifts to longer wavelengths at different rates for the three dye molecules. The shift is complete fastest for the DN91 sensitised solar cell, slower for DN216 and slowest for DN285. Although Stark shifts have been reported for indoline-dye sensitised solar cells [43; 44], we believe the shift is simply a representation of the different rates at which the signals decay. At the fringe between the GSB and ESA+OX signals (approximately 600 nm) there is a superposition of the two signals, one negative and the other positive. Therefore as the ultrafast ESA signal decays, the fringe is dominated by the GSB. Of course, as the ESA signal decays at different rates for the different dyes, this will have an impact on the apparent shift of the GSB signal into the fringe region.

5.5 Applied Voltage Measurements

Measurements were taken on the three DSSC samples each sensitised with one of the indoline dyes DN91, DN216 and DN285 under applied voltage conditions. This was done to determine if applying an external potential of +/- 1V to the cells (sufficient to increase current flow significantly or stop all flow of current) had an effect on the charge transfer processes, especially the ultrashort injection times. The measured short and long time window transient absorption spectra were compared and no differences observed. The ESA, OX and GSB signals are once again present, at the same central wavelengths as seen previously. By taking horizontal lineouts of the ESA+OX signal for the three dyes and fitting them, we can compare the effect of the applied external potentials on the injection times for the three dyes, see figure 5.12.

The traces and bi-exponential fits in the main graphs have been shifted by 0.1 vertically for a clearer view of the three decays. The inserts show the unshifted traces, from which it is very clearly observable that applying an external potential has no effect on the injection times and relative amplitudes of any of the three dyes. Therefore the least noisy UTA spectra were used for the investigation of the effect of the alkyl chain length on injection efficiencies, section 5.1.

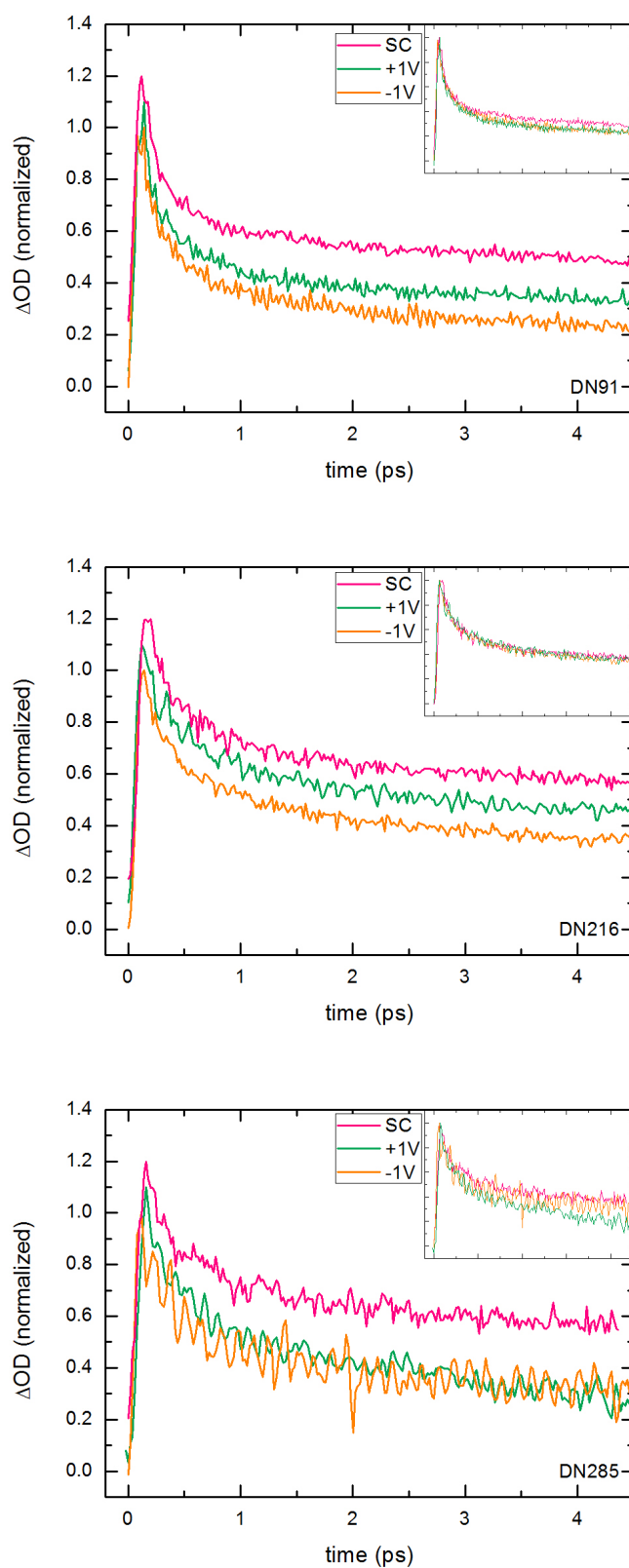


Figure 5.12: The short window ESA temporal traces taken at 680 nm from transient absorption spectra measured under **SC** (pink), **+1V** (green) and **-1V** (orange) conditions for three different samples each sensitised with one of the indoline dyes DN285 (top), DN216 (centre) and DN91 (bottom). The three decays are shifted vertically from each other by 0.1 units in the main graphs, and plotted with no shift in the inserts.

6. Conclusion

Although not as efficient as silicon solar cells, organic-dye sensitised solar cells continue to be interesting as they are cost effective and easy to make. Fully operational DSSC samples were made by electrodeposition of ZnO and sensitised with one of three indoline dyes, different from one another only in the alkyl chain length bonded to one of two carboxyl anchors. The hope was that the second anchor will stabilise the dye-ZnO bonding and positively contribute to the charge transfer between them. The results were put into perspective with previous results on D149-ZnO cells wherein the dye has only one -COOH anchor group.

From the I-V curves, we observed that the short circuit current density J_{SC} is dependent on the alkyl chain length of the dye molecule – as it increases with decreasing chain length. As expected, the open circuit voltage V_{OC} remains constant (~ 0.6 V) for all three types of samples, showing good cell reproducibility.

With the use of ultrafast transient absorption spectroscopy we measured charge transfer dynamics within the DSSCs and were able to attribute the trend in J_{SC} values to the same trend in injection efficiencies for the three dyes. This was done by fitting the signals observed in the transient absorption spectra with exponential decay functions and extracting the time constants as well as corresponding amplitudes and assigning them to the various phases of the charge dynamics after photoexcitation. Therefore allowing us to determine how fast a state is filled or depleted, as well as the relative number of electrons being transferred in these processes.

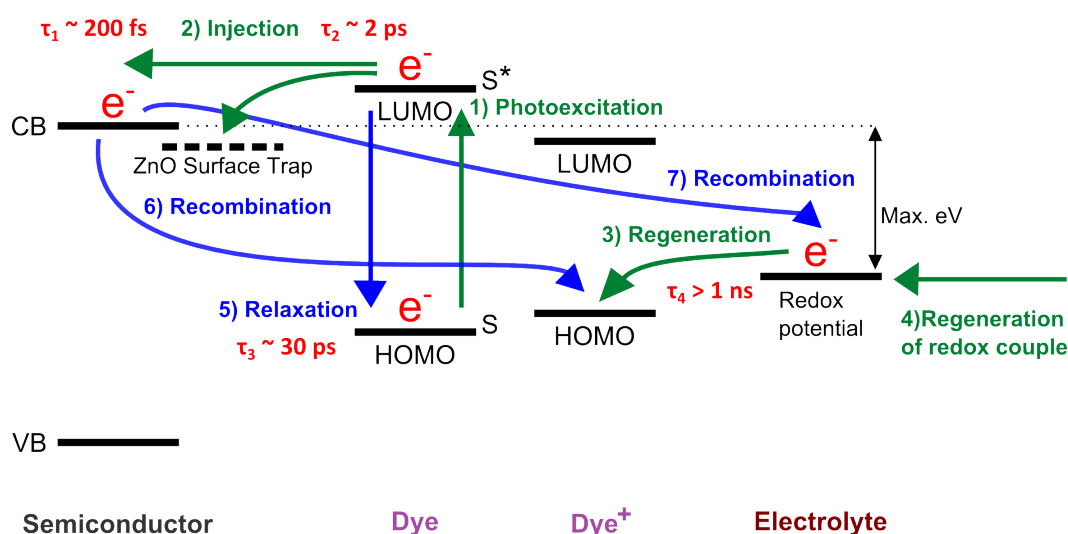


Figure 6.1: Summary of the charge transfer processes which occur in a DSSC. Optimal processes are marked in green, counter process in blue and the processes not measured using TAS have been grayed out.

From the results, we observed four time constants with corresponding relative amplitudes (the sum of which was normalised to 1) for the superposition of the excited state absorption (ESA) of the neutral dye signal and the oxidised dye absorption (OX) signal, see figure 6.1. The four process were interpreted to be the depletion of the ESA by injection of electrons to the ZnO conduction band (~ 200 fs), injection of electrons to ZnO surface trap states (~ 2 ps), and relaxation of photoexcited electrons back to the ground state (~ 30 ps). The OX signal decays with a longer time constant than we are able to measure (> 1 ns) as it is regenerated by

electron transfer from the redox couple in the electrolyte. The two longer processes replenish the ground state bleaching (GSB) and are also found in the GSB signal decay.

The decay times and amplitudes were then compared and we found the following: DN91 (shortest alkyl chain) has the most efficient injection to the ZnO conduction band – fastest time and largest amplitude, followed by DN216, and DN285 (longest alkyl chain) has the least efficient injection – slowest time and lowest amplitude. These amplitudes are supported by the OX signal amplitudes as a more efficient injection creates a larger number of oxidised dye molecules.

Moreover, the most efficient injection is supported by the highest J_{SC} , while the least efficient injection by the lowest J_{SC} . Intuitively, this can be explained as the more electrons are injected into the ZnO conduction band efficiently, the higher current can be extracted from the cell. What may not be as intuitive is the second injection to the ZnO surface trap states which was found to be on the same time scale for all three dyes (~ 2 ps), but occurred with decreasing amplitude as the chain length shortened: A_2 (DN285) $>$ A_2 (DN216) $>$ A_2 (DN91). While the trend in amplitudes can be explained as the reverse of the initial ultrafast injection efficiency, the rate of the injection (approximately 2 ps for all three dyes) seems to be independent of the alkyl chain length, suggesting an injection mechanism which does not occur through the carboxyl anchor.

Naturally, the more electrons are injected (through both possible pathways), the less electrons are available for non-radiative relaxation. Therefore a high $A_1 + A_2$ sum will lead to a low A_3 amplitude, as in the case of DN91 and vice versa, as in the case of DN285. The observed charge dynamics in DN285-ZnO are very similar to those of the D149 cell, confirming that a second anchor improves electron injection, if it is not too far from the chromophore by the alkyl chain. The first hope of increased stability, could be impressively confirmed with cell lifetimes of months compared to the D149 cells.

Further measurements that can still be taken on these particular DSSC samples are with the use of a white light probe pulse stretching into the infra-red spectral range. In this way the absorption of the electrons in the ZnO conduction band can be probed and we would have more information on the injection path and time constants of the photoexcited electrons into ZnO.

Driven by the chase to higher solar cell efficiencies, perovskite solar cells were developed with both ZnO and TiO_2 as the semiconductor. Here the donor and acceptor are organic molecules in condensed phase, removing the liquid electrolyte and dye aggregates from the scheme. Although still relatively new, high efficiencies and open circuit voltages have been extracted from these cells. With the use of transient absorption spectroscopy we may be able to learn more about the charge transfer processes and aid in the development of better light harvesting devices.

In general, as the need for alternate energy sources grows, solar cells will be relied on to play an increasingly important role in providing electricity to the Earth's energy grid.

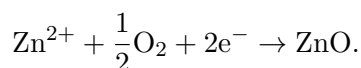
Appendices

A. Experimental Details of Fabrication of DSSCs

The electrodeposition of ZnO thin films and subsequent making of fully operational DSSCs was done on activated $250 \times 300 \times 22$ mm FTO (Fluorine-doped Tin Oxide) coated glass substrates [24; 27; 42].

Firstly the glass slides were washed in a soap solution followed by acetone and isopropanol and rinsed with deionised water and dried with N_2 gas in between each rinse. Then, the FTO was activated by submerging the glass slide in nitric acid for 2 minutes and rinsed with deionised water and dried once again with N_2 gas. The glass substrate was then placed FTO side-up in a home-made sample mount and contacted with a copper tape. After which, a chosen $\pi \text{ cm}^2$ area was stamped out of a strong adhesive masking tape. This was used to seal the copper contacts while exposing the $\pi \text{ cm}^2$ area of FTO to the electrodeposition solution.

The deposition bath, consisting of 0.1 M KCl aqueous solution, was heated at 70°C and oxygenated by pumping of oxygen gas at $40 \text{ mL}\cdot\text{min}^{-1}$. The sample was then submerged in the electrodeposition solution and rotated at 500 rpm with the use of a rotating disk electrode. The FTO was activated electrochemically in the KCl bath for 15 minutes in a three electrode system. A Pt wire was used as the counter electrode and a voltage of -1160 mV was applied versus a Ag/AgCl reference electrode. This was immediately followed by the electrodeposition of the ZnO blocking layer for 10 minutes with a Zn wire counter electrode and a concentration of 5 mM ZnCl_2 in the deposition bath. An external voltage of -1060 mV vs Ag/AgCl was used for this process. Finally, for the electrodeposition of a porous ZnO layer, a 300 μM eosinY environment was used with a deposition time of 5 minutes and an applied potential of -960 mV vs Ag/AgCl. ZnO formation in an oxygenated system occurs according to:



The samples were left to cool to room temperature in deionised water preheated to 70°C , after which they were rinsed with room temperature deionised water and dried with N_2 gas. To desorb the eosinY dye from within the ZnO pores, the substrates were submerged in a KOH aqueous solution with pH 10.5 overnight. Before the porous ZnO thin films could be sensitised, the excess water was evaporated from the ZnO surface by heating the substrates at 150°C for 30 minutes. The films were then exposed to a UV lamp for a further 30 minutes to facilitate the presence of OH groups on the ZnO surface which aid with indoline dye adsorption. For the sensitisation, the substrates were immersed for 1 minute in indoline dye solutions (DN285, DN216 and DN91) made up as 0.5 mM dye in 1 mM lithocholic acid. Once sensitised, the thin films were washed in ethanol and dried with N_2 gas.

Sandwich cells were then made following the process of chapter 3. Before the counter electrodes ($250 \times 350 \times 22$ mm FTO coated glass slides) were sputter-deposited with 5 mM ethanoic solution of hexachloroplatinic acid and baked at 450°C for 30 minutes, the slides were washed with soap solution, acetone and isopropanol and rinsed with deionised water and dried with N_2 gas in between each rinse. For the electrolyte, 0.5 M 1-methyl-3-propylimidazolium iodide and 0.05 M I_2 in acetonitrile was used, and dropped through one of the two pre-drilled holes in the counter electrode which were then sealed with glass and sealing foil.

B. Self Phase Modulation

The self phase modulation responsible for white light generation can be calculated from the electric field of the incoming wave and the refractive index of the sapphire crystal [39; 40; 45]. If the electric field of the incoming light pulse is given as $E(z, t) = E_0(z, t)\exp(ik_0z - i\omega_0t)$, it can be rewritten as $E = E_0e^{i\phi}$ where ϕ is the time dependent phase and it is given by $\phi(t) = k_0z - \omega_0t$.

By using the definition of the wavenumber, $k_0 = \frac{2\pi}{\lambda_0} = \frac{\omega_0}{v} = \frac{n\omega_0}{c}$, the following expression for the phase can be obtained by substitution:

$$\phi(t) = \frac{n(t)\omega_0z}{c} - \omega_0t$$

If the laser pulse intensity is very high and I is time dependent then n becomes $n(r, t)$ due to the intensity profile in time and space of I . Substituting $n(r, t) = n_0 + n_2I(r, t)$ then yields an equation for the phase modulation of the pulse:

$$\phi(t) = \frac{n_0\omega_0z}{c} + \frac{n_2I(t)\omega_0z}{c} - \omega_0t$$

From the above equation, it can be seen that the phase modulation is proportional to the laser pulse intensity. A plot of phase versus time will therefore have the same Gaussian shape as the laser pulse time dependent intensity (square of the electric field), see figure B.1.

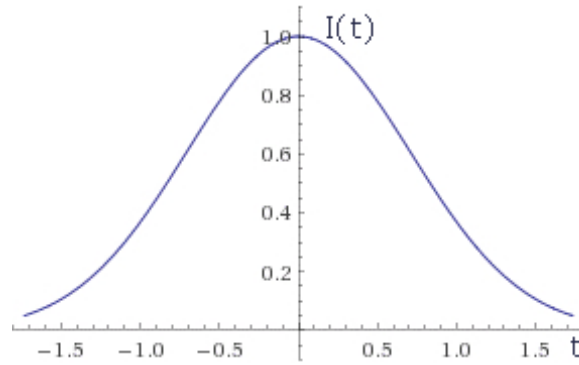


Figure B.1: Gaussian function serving as a representation of the laser pulse intensity distribution, or laser pulse phase plotted against time.

The instantaneous frequency of the light pulse is calculated as a time derivative of the phase as

$$\omega(t) = -\frac{d\phi}{dt} = \omega_0 - \frac{n_2\omega_0z}{c} \frac{dI}{dt}$$

The new frequencies created in the white light generation process are determined by the above equation and therefore depend on the time derivative of the laser beam intensity (see figure B.2). In this way, a phase modulation leads to a frequency modulation.

From figure B.3, we can see that an increase in intensity leads to a decrease in frequency (red shift) and a decrease in intensity leads to an increase in frequency (blue shift).

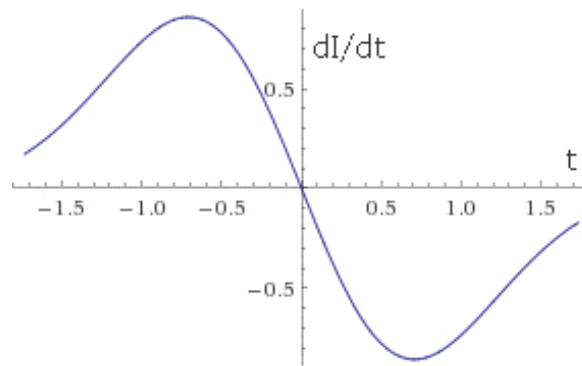


Figure B.2: An example plot of the derivative of a Gaussian function (the time derivative of the laser pulse intensity) is shown.

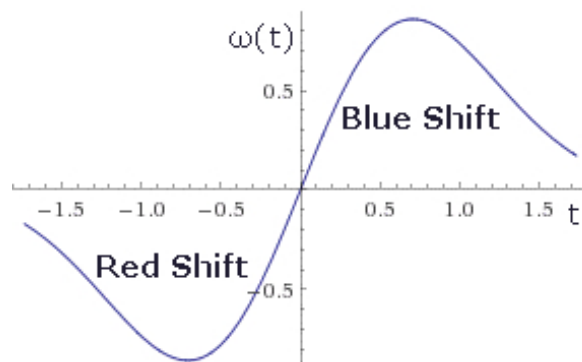


Figure B.3: An example plot of the negative derivative of a Gaussian function (the negative time derivative of the laser pulse intensity) is shown. SPM results in a red shift at early times (front of the pulse) and a blue shift at later times (back of the pulse).

Bibliography

- [1] Hagfeldt, A., Boschloo, G., Sun, L., Kloo, L. and Pettersson, H.: Dye-Sensitized Solar Cells. *Chemical Reviews*, vol. 110, no. 11, pp. 6595–6663, November 2010.
- [2] Vallejo L, W.A., Quinones S, C.A. and Hernandez S, J.A.: The chemistry and physics of dye-sensitized solar cells. In: *Solar Cells - Dye-Sensitized Devices*. InTech, November 2011.
- [3] Shrestha, S.: Photovoltaics literature survey (No. 112). *Prog. Photovolt: Res. Appl.*, vol. 22, no. 8, pp. 933–936, July 2014.
- [4] Green, M.A., Emery, K., Hishikawa, Y., Warta, W. and Dunlop, E.D.: Solar cell efficiency tables (version 44). *Prog. Photovolt: Res. Appl.*, vol. 22, no. 7, pp. 701–710, June 2014.
- [5] Wenham, S.R. and Green, M.A.: Silicon solar cells. *Prog. Photovolt: Res. Appl.*, vol. 4, no. 1, pp. 3–33, January 1996.
- [6] Kojima, A., Teshima, K., Shirai, Y. and Miyasaka, T.: Organometal Halide Perovskites as Visible-Light Sensitizers for Photovoltaic Cells. *Journal of the American Chemical Society*, vol. 131, no. 17, pp. 6050–6051, May 2009.
- [7] Burschka, J., Pellet, N., Moon, S.-J., Humphry-Baker, R., Gao, P., Nazeeruddin, M.K. and Grätzel, M.: Sequential deposition as a route to high-performance perovskite-sensitized solar cells. *Nature*, vol. 499, no. 7458, pp. 316–319, July 2013.
- [8] Marchioro, A., Teuscher, J., Friedrich, D., Kunst, M., van de Krol, R., Moehl, T., Grätzel, M. and Moser, J.-E.: Unravelling the mechanism of photoinduced charge transfer processes in lead iodide perovskite solar cells. *Nature Photon*, vol. 8, no. 3, pp. 250–255, January 2014.
- [9] Mathew, S., Yella, A., Gao, P., Humphry-Baker, R., Curchod, B.F.E., Ashari-Astani, N., Tav-ernelli, I., Rothlisberger, U., Nazeeruddin, M.K. and Grätzel, M.: Dye-sensitized solar cells with 13% efficiency achieved through the molecular engineering of porphyrin sensitizers. *Nat Chem*, vol. 6, no. 3, pp. 242–247, February 2014.
- [10] Wang, M., Grätzel, C., Zakeeruddin, S.M. and Grätzel, M.: Recent developments in redox electrolytes for dye-sensitized solar cells. *Energy Environ. Sci.*, vol. 5, no. 11, p. 9394, 2012.
- [11] Chung, I.I., Lee, B.B., He, J.J., Chang, R.P.H.R. and Kanatzidis, M.G.M.: All-solid-state dye-sensitized solar cells with high efficiency. *Nature*, vol. 485, no. 7399, pp. 486–489, May 2012.
- [12] Yella, A., Lee, H.W., Tsao, H.N., Yi, C., Chandiran, A.K., Nazeeruddin, M.K., Diao, E.W.G., Yeh, C.Y., Zakeeruddin, S.M. and Grätzel, M.: Porphyrin-Sensitized Solar Cells with Cobalt (II/III)-Based Redox Electrolyte Exceed 12 Percent Efficiency. *Science*, vol. 334, no. 6056, pp. 629–634, November 2011.
- [13] El-Zohry, A., Orthaber, A. and Zietz, B.: Isomerization and Aggregation of the Solar Cell Dye D149. *J. Phys. Chem. C*, vol. 116, no. 50, pp. 26144–26153, December 2012.
- [14] O'Regan, B. and Grätzel, M.: A low-cost, high-efficiency solar cell based on dye-sensitized colloidal TiO₂ films. *Nature*, vol. 353, no. 6346, pp. 737–740, October 1991.

- [15] Ooyama, Y. and Harima, Y.: Photophysical and Electrochemical Properties, and Molecular Structures of Organic Dyes for Dye-Sensitized Solar Cells. *ChemPhysChem*, vol. 13, no. 18, pp. 4032–4080, July 2012.
- [16] De Angelis, F., Fantacci, S., Selloni, A., Grätzel, M. and Nazeeruddin, M.K.: Influence of the Sensitizer Adsorption Mode on the Open-Circuit Potential of Dye-Sensitized Solar Cells. *Nano Lett.*, vol. 7, no. 10, pp. 3189–3195, October 2007.
- [17] Nazeeruddin, M.K., De Angelis, F., Fantacci, S., Selloni, A., Viscardi, G., Liska, P., Ito, S., Takeru, B. and Grätzel, M.: Combined Experimental and DFT-TDDFT Computational Study of Photoelectrochemical Cell Ruthenium Sensitizers. *Journal of the American Chemical Society*, vol. 127, no. 48, pp. 16835–16847, December 2005.
- [18] Anta, J.A., Guillén, E. and Tena-Zaera, R.: ZnO-Based Dye-Sensitized Solar Cells. *J. Phys. Chem. C*, vol. 116, no. 21, pp. 11413–11425, May 2012.
- [19] Le Bahers, T., Pauporté, T., Scalmani, G., Adamo, C. and Ciofini, I.: A TD-DFT investigation of ground and excited state properties in indoline dyes used for dye-sensitized solar cells. *Phys. Chem. Chem. Phys.*, vol. 11, no. 47, pp. 11276–11284, 2009.
- [20] Ito, S., Miura, H., Uchida, S., Takata, M., Sumioka, K., Liska, P., Comte, P., Péchy, P. and Grätzel, M.: High-conversion-efficiency organic dye-sensitized solar cells with a novel indoline dye. *Chem. Commun.*, vol. 0, no. 41, pp. 5194–5196, 2008.
- [21] Matsui, M., Ito, A., Kotani, M., Kubota, Y., Funabiki, K., Jin, J., Yoshida, T., Minoura, H. and Miura, H.: The use of indoline dyes in a zinc oxide dye-sensitized solar cell. *Dyes and Pigments*, vol. 80, no. 2, pp. 233–238, February 2009.
- [22] Higashijima, S., Miura, H., Fujita, T., Kubota, Y., Funabiki, K., Yoshida, T. and Matsui, M.: Highly efficient new indoline dye having strong electron-withdrawing group for zinc oxide dye-sensitized solar cell. *Tetrahedron*, vol. 67, no. 34, pp. 6289–6293, August 2011.
- [23] Higashijima, S., Inoue, Y., Miura, H., Kubota, Y., Funabiki, K., Yoshida, T. and Matsui, M.: Organic dyes containing fluorene -substituted indoline core for zinc oxide dye-sensitized solar cell. *RSC Advances*, vol. 2, no. 7, pp. 2721–2724, 2012.
- [24] Yoshida, T., Zhang, J., Komatsu, D., Sawatani, S., Minoura, H., Pauporté, T., Lincot, D., Oekermann, T., Schlettwein, D., Tada, H., Wöhrle, D., Funabiki, K., Matsui, M., Miura, H. and Yanagi, H.: Electrodeposition of Inorganic/Organic Hybrid Thin Films. *Adv. Funct. Mater.*, vol. 19, no. 1, pp. 17–43, 2009.
- [25] Strothkämper, C., Bartelt, A., Sippel, P., Hannappel, T., Schütz, R. and Eichberger, R.: Delayed Electron Transfer through Interface States in Hybrid ZnO/Organic-Dye Nanostructures. *J. Phys. Chem. C*, vol. 117, no. 35, pp. 17901–17908, 2013.
- [26] Falgenhauer, J., Richter, C., Miura, H. and Schlettwein, D.: Stable Sensitization of ZnO by Improved Anchoring of Indoline Dyes. *ChemPhysChem*, vol. 13, no. 12, pp. 2893–2897, June 2012.
- [27] Ichinose, K., Kimikado, Y. and Yoshida, T.: The effect of pre-treatments of f-doped SnO₂ substrates for cathodic nucleation of ZnO crystals in aqueous ZnCl₂ solution with dissolved O₂. *Electrochemistry*, vol. 79, no. 3, pp. 146–155, 2011.
- [28] Magne, C., Urien, M. and Pauporté, T.: Optimization of electrochemically grown dense ZnO/nanoporous ZnO stacked structures for dye-sensitized solar cell application. *Physica Status Solidi B*, vol. 250, no. 10, pp. 2126–2131, July 2013.
- [29] Mandal, G., Bhattacharya, S., Chowdhury, J. and Ganguly, T.: Mode of anchoring of ZnO nanoparticles to molecules having both –COOH and –NH functionalities. *Journal of Molecular Structure*, vol. 964, no. 1–3, pp. 9–17, February 2010.

- [30] Sakuragi, Y., Wang, X.-F., Miura, H., Matsui, M. and Yoshida, T.: Aggregation of indoline dyes as sensitizers for ZnO solar cells. *Journal of Photochemistry and Photobiology A: Chemistry*, vol. 216, no. 1, pp. 1–7, November 2010.
- [31] Halme, J., Vahermaa, P., Miettunen, K. and Lund, P.: Device Physics of Dye Solar Cells. *Adv. Mater.*, vol. 22, no. 35, pp. E210–E234, August 2010.
- [32] Zhang, S., Yang, X., Numata, Y. and Han, L.: Highly efficient dye-sensitized solar cells: progress and future challenges. *Energy Environ. Sci.*, vol. 6, no. 5, pp. 1443–1464, 2013.
- [33] Bisquert, J. and Marcus, R.A.: Device Modeling of Dye-Sensitized Solar Cells. In: *link.springer.com*, pp. 325–395. Springer Berlin Heidelberg, Berlin, Heidelberg, September 2013.
- [34] Jose, R., Kumar, A., Thavasi, V., Fujihara, K., Uchida, S. and Ramakrishna, S.: Relationship between the molecular orbital structure of the dyes and photocurrent density in the dye-sensitized solar cells. *Applied Physics Letters*, vol. 93, no. 2, p. 023125, July 2008.
- [35] Megerle, U., Pugliesi, I., Schrieber, C., Sailer, C.F. and Riedle, E.: Sub-50 fs broadband absorption spectroscopy with tunable excitation: putting the analysis of ultrafast molecular dynamics on solid ground. *Appl. Phys. B*, vol. 96, no. 2-3, pp. 215–231, June 2009.
- [36] Riedle, E., Beutter, M., Lochbrunner, S., Piel, J., Schenkl, S., Spörlein, S. and Zinth, W.: Generation of 10 to 50 fs pulses tunable through all of the visible and the NIR. *Appl. Phys. B*, vol. 71, no. 3, pp. 457–465, February 2014.
- [37] Riedle, E.: *NOPA Fundamentals and Instructions*. University of Munich, April 2005.
- [38] Fork, R.L., Shank, C.V., Hirlimann, C., Yen, R. and Tomlinson, W.J.: Femtosecond white-light continuum pulses. *Optics Letters*, vol. 8, no. 1, pp. 1–3, 1983.
- [39] Jarman, C., Schumacher, D., Modoran, C., Harmon, N. and Yoscovits, Z.: Supercontinuum Generation in Sapphire: A Measurement of Intensity. Tech. Rep., 2005.
- [40] Alfano, R.R. (ed.): *The Supercontinuum Laser Source*. Fundamentals with Updated References, 2nd edn. Springer, 2006.
- [41] Zheltikov, A.M.: Let there be white light: supercontinuum generation by ultrashort laser pulses. *Physics-Uspekhi*, vol. 49, no. 6, p. 605, 2006.
- [42] Rohwer, E., Richter, C., Heming, N., Strauch, K., Litwinski, C., Nyokong, T., Schlettwein, D. and Schwoerer, H.: Ultrafast Photodynamics of the Indoline Dye D149 Adsorbed to Porous ZnO in Dye-Sensitized Solar Cells. *ChemPhysChem*, vol. 14, no. 1, pp. 132–139, 2013.
- [43] Burdziński, G., Karolczak, J. and Ziółek, M.: Dynamics of local Stark effect observed for a complete D149 dye-sensitized solar cell. *Phys. Chem. Chem. Phys.*, vol. 15, no. 11, p. 3889, February 2013.
- [44] Oum, K., Lohse, P.W., Flender, O., Klein, J.R., Scholz, M., Lenzer, T., Du, J. and Oekermann, T.: Ultrafast dynamics of the indoline dye D149 on electrodeposited ZnO and sintered ZrO₂ and TiO₂ thin films. *Phys. Chem. Chem. Phys.*, vol. 14, no. 44, pp. 15429–15437, 2012.
- [45] Ashcom, J.B.: *The role of focusing in the interaction of femtosecond laser pulses with transparent materials*. Ph.D. thesis, Harvard University, January 2003.